LUND UNIVERSITY

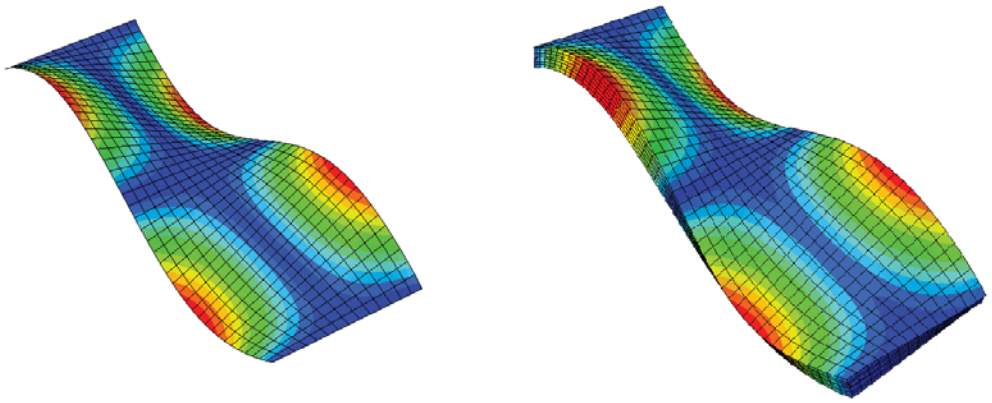

DYNAMIC RESPONSE OF CROSS LAMINATED TIMBER FLOORS SUBJECT TO INTERNAL LOADS

JACOB SKOGLUND

Structural Mechanics

Master's Dissertation

DEPARTMENT OF CONSTRUCTION SCIENCES
DIVISION OF STRUCTURAL MECHANICS

ISRN LUTVDG/TVSM--20/5244--SE (1-54) | ISSN 0281-6679
MASTER'S DISSERTATION

DYNAMIC RESPONSE OF CROSS LAMINATED TIMBER FLOORS SUBJECT TO INTERNAL LOADS

JACOB SKOGLUND

Supervisor: Dr **PETER PERSSON**, Division of Structural Mechanics, LTH.
Assistant Supervisor: Dr **HENRIK DANIELSSON**, Division of Structural Mechanics, LTH.
Examiner: Professor **ERIK SERRANO**, Division of Structural Mechanics, LTH.

Printed by V-husets tryckeri LTH, Lund, Sweden, June 2020 *(Pl)*.

For information, address:
Division of Structural Mechanics,
Faculty of Engineering LTH, Lund University, Box 118, SE-221 00 Lund, Sweden.
Homepage: www.byggmek.lth.se

Abstract

The deregulation of timber for use in large scale constructions has seen the addition of new innovative timber-based products to a category of products referred to as *engineered wood products*. A now well established addition to these products is cross laminated timber, or CLT for short. CLT products use a form of orthogonal layering, where several parallel wooden boards are arranged in a number of layers, each layer being orthogonal to the previous. The use of orthogonal layering allows for increased stiffness in the two plane directions, resulting in a lightweight construction product with high load bearing capacity and stiffness.

To evaluate the dynamic behaviour of structures, engineers commonly apply the finite element method, where a system of equations are solved numerically. Given a sufficient amount of computational power and time, the finite element method can help to solve most dynamical problems. For sufficiently large or complex structures the amount of resources needed may be outside the scope of possibility or feasibility for many. Therefore, evaluating the usage of certain design simplifications, such as omitting to models aspects of the geometry, or alternative forms of analysis for CLT panels may help to reduce the time and resources required for an analysis.

In this Master's dissertation, a seven-layer CLT-panel has been created. In the model, each individual board and the gaps between the boards are modelled. The seven-layer model is used as a reference to evaluate the possibility of using less detailed alternative models. The alternative models are created as a layered 3D model and a composite 2D model, both models omit the modelling of the individual laminations, resulting in the layers being solid.

The results show small errors for the alternative models when using modal analysis. Concluding that the modal behaviour and dynamic response of a CLT panel can be evaluated using a composite 2D model or a less-detailed layered 3D model. This significantly reduces the amount of time and computational power needed for an analysis, and clearly indicates the benefit of using alternative less detailed models.

Acknowledgement

This Master's dissertation was performed and carried out at the Division of Structural Mechanics at LTH. It concludes my fifth and last year studying engineering at Lund University.

Given the restrictions and difficulties of communication due to the Covid-19 pandemic, I want to thank my supervisors Dr Peter Persson & Dr Henrik Danielsson whose guidance, support and insight have been essential to the realisation of this dissertation.

Also, I want to thank my parents whose unconditional support, both mental and financial, have helped me overcome every hurdle I've faced during these five years.

Symbols

Mathematical operators

Symbol	Description
$\square^T$	Transpose
$\int_S$	Surface integral
$\int_V$	Volume integral
$\square_i$	Vector
$\square_{ij}$	Matrix

Greek

Symbol	Description
σ	Stress
ε	Strains
ϕ_n	n:th natural mode
ω_n	n:th natural frequency [rads/s]
Φ_{ij}	Modal matrix
ζ	Damping ratio
ζ_n	Damping ration n:th mode
ν	Poisson's ratio
ρ	Density

Roman

Symbol	Description
L	Longitudinal
R	Radial
T	Tangential
V	Volume
S	Surface
A	Area
E	Young's modulus
G	Shear modulus
n_i	Normal vector
D_{ij}	Constitutive matrix
C_{ij}	Flexibility matrix
b_i	Body weight vector
t_i	Traction vector
P_i	Force vector
u_i	Displacement vector
$\ddot{u}_i$	Acceleration vector
v_i	Arbitrary weight vector
N_i	Global shape function
B_{ij}	Global deformation matrix
$\mathbf{M}$	Mass matrix
$\mathbf{K}$	Stiffness matrix
q_n	n:th modal cordinate
T_n	n:th natural period [Hz^{-1}]
f_n	n:th natural frequency [Hz]
a_0	Mass proportional damping
a_1	Stiffness proportional damping

Contents

Abstract I
Acknowledgement II
Symbols IV

1 Introduction **1**
1.1 Background 1
1.2 Aim and objective 2
1.3 Method 2
1.4 Limitations 3

2 Cross laminated timber **5**
2.1 Background 5
2.2 Manufacturing 5
2.3 Finger joints 6
2.4 Sustainability 6

3 Material properties of wood **7**
3.1 Anatomy 7
3.1.1 Micro scale 8
3.1.2 Anomalies 9
3.2 Orthotropic behaviour 9

4 Structural dynamics **11**
4.1 Equation of motion 11
4.1.1 Strong formulation 11
4.1.2 Weak formulation 12
4.2 Finite element method 12
4.2.1 FE-formulation of motion 13
4.3 Calculation of eigenmodes 14
4.4 Classically damped system 15
4.5 Modal analysis of classically damped systems 16
4.6 Steady state dynamic analysis 18
4.7 Evaluation metrics 18
4.7.1 Root mean square 18
4.7.2 Normalised relativ frequency difference 18
4.7.3 Percentage error 19

4.7.4 Velocity error . . . 19

5 Numerical models **21**
5.1 High-fidelity 3D model . . . 21
5.2 Layered 3D model . . . 23
5.3 Composite 2D model . . . 24
5.4 Validation of model . . . 25

6 Effect on dynamic properties **27**
6.1 High-fidelity 3D model . . . 27
6.2 Layered 3D model . . . 29
6.3 Composite 2D model . . . 31
6.4 Differences in dynamic properties . . . 33

7 Effects on dynamic response **35**
7.1 Damping . . . 35
7.2 Direct solution - Effects on mobilities . . . 36
7.2.1 Load position 1 . . . 36
7.2.2 Load position 2 . . . 38
7.3 Alternative analysis . . . 40
7.3.1 Rayleigh damping . . . 40
7.3.2 Direct modal damping . . . 43
7.4 Response differences . . . 45

8 Discussion **47**
8.1 Dynamic properties . . . 47
8.2 Dynamic response . . . 47
8.3 General discussion . . . 48

9 Conclusion **49**
9.1 Summary of results . . . 49
9.2 Future work . . . 49

Bibliography **51**

1 Introduction

1.1 Background

The early 20^{th} century saw the decline of classical timber constructions for buildings exceeding two storeys in most urban environments, instead, the construction industry turned to the use of reinforced concrete. A cheap, robust and far less combustible material, reinforced concrete has dominated the industry since its introduction and still does so to this day [3].

The first sign of change to the concrete construction trend came with the addition of new timber alternatives. Countries around the alps, whom largely had transitioned to concrete, imagined that the rich woodland that lined their mountainous valleys, could, with modern technology, constitute the base of a new construction material. Towards the end of the 1990s Austrian scientists introduced CLT, or Cross laminated timber, panels [2]. CLT panels consists of a multitude of layers of laminated timber boards put parallel to one another, where each layer is ordered orthogonal to the previous, see Figure 1.1. Usually manufactured in an odd number of layers so that the bottom and top layer are parallel, helping to bolster the panels strength. Each board is connected to its neighbor by an adhesive, but there also exists CLT boards manufactured using screws or nails [19]. Although a light construction product, CLT panels boost excellent strength and stiffness properties, allowing for construction of larger structures such as high-rise buildings or arenas. The engineering and architectural constructional possibilities are heavily amplified by large manufacturing freedoms in cross section and length. As a result, CLT panels can serve a variety of construction purposes both aesthetic and load-bearing [2].

The usage of wood as a building material has steadily been increasing, with many considering it architecturally appealing. In terms of dynamic behaviour, the usage of

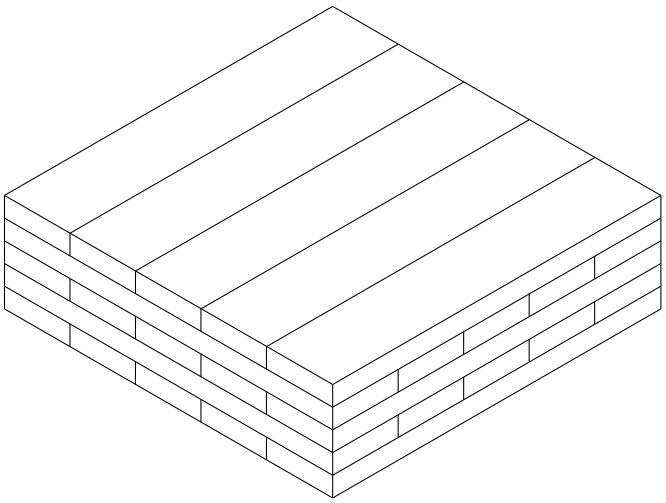

Figure 1.1: Illustration of a CLT panel.

lightweight timber buildings results in wave propagation at a lower frequency range than for conventional building materials like concrete or steel. Lower frequency sounds are perceived as more irritating for occupants, and currently only some timber structures achieve acoustic comfort [11].

A common approach to evaluating the behaviour of structures is a numerical approach through the finite element (FE) method. The FE method has the added benefit of allowing a large degree of design freedom, since material parameters, load scenarios, boundary conditions and dimensions can easily be altered and adjusted. Any CLT structure could therefore be modelled and evaluated using the FE method before its construction or installation. Programs applying the FE method require increased computational power when the dimension or amount of details are increased. To reduce the computational power necessary for an analysis, simplifications in terms of both geometry and type of analysis are often evaluated.

1.2 Aim and objective

The aim of the Master's dissertation is to broaden the understanding of the dynamical response of CLT panels subject to different loads. By using a FE-modelling software, a detailed high-fidelity model will be used to determine the dynamic response of a CLT panel, acting as a reference model. The objective is to determine whether a computationally less requiring and, in terms of design, more time efficient model can be used to replicate the same dynamic response as the reference model. The report will thus inquire into:

- Can a more time-efficient model replicate the modal behaviour of the 3D high-fidelity model.
- Can the same models replicate the dynamic response of a CLT panel subject to internal loads directly affecting the panel, such as walking or influence from furniture.
- The feasibility of using less detailed models to replicate the dynamic behaviour of a 3D model.

Determining the feasibility of using alternative models to replicate the dynamic behaviour of CLT structures, may help to identify what forms of assumptions and simplifications can be made when designing numerical CLT models.

1.3 Method

The modeling and numerical analysis will be performed in the finite element software ABAQUS CAE. A reference model of a CLT-panel will be constructed and the

eigenfrequencies determined. To ensure the validity of the reference model, the eigenfrequencies will be compared to published results in scientific journals.

Once the reference model has been validated, the model will be subject to various internal loads and the dynamic response determined. The dynamic response of the reference model will then be used to develop a more time efficient model that reliably mimics these results, without requiring the same amount of computational power.

1.4 Limitations

This Master's dissertation focuses on numerical modelling approaches for CLT floors. Aimed at performing a comparative dynamic analysis for three different models, the models are designed using different modelling approaches to achieve the same dynamic behaviour. In the dissertation, the following effects are assumed to give a negligible influence on the conclusions:

- Anomalies and external effects such as moisture, knots, fibre misalignment, cracks etc.
- Non-linear elastic behaviour such as creep.

.

2 Cross laminated timber

Cross laminated timber (or CLT) is a common name for timber panels constructed by numerous layers of wooden boards, where each layer is oriented orthogonal to the adjacent layer. The orthogonal layering has the added benefit of making CLT panels bi-dimensional elements, capable of resisting any form of bending parallel to the plane axis [6]. This, accompanied by good load bearing capacity and high stiffness, compared to other lightweight products, makes CLT panels suitable as both floor structures and load bearing walls. In comparison to other building products, such as reinforced concrete or steel, CLT panels are very light. For constructions of both a simple and complex nature, lightweight products are more easily transported and assembled [2].

2.1 Background

Timber has historically held an important position for construction through much of the world. Yet, the combustible nature of timber, in combination with rapid increase in urbanisation, necessitated a change towards less combustible building materials. Most countries opted for the usage of mineral based materials such as concrete or bricks, enforcing legislative restrictions on the use of timber as a building material. Sweden had experienced vast devastation due to timber related fires during the early 19^{th} century, most famously the complete destruction of Karlstad in 1865. These timber related fires resulted in limiting the construction of wooden structures to no more than two storeys in 1874 [18]. Construction during the 20^{th} century would instead be defined by the emergence of reinforced concrete and steel on a global scale. While timber would be relegated to only smaller lightweight structures and buildings [3].

Concrete and steel still remain as the leading construction material throughout much of the world. Yet, innovation and political interest in timber as a construction material has seen the introduction of new viable timber alternatives. The woodland rich central European nations of the Alps tasked themselves with the modernisation of timber for construction purposes in the 1990s. As a result, research effort, most importantly in Austria, led to the introduction of CLT panels to the public [2].

2.2 Manufacturing

Anomalies, such as branches or knots, along with the natural growth limit of trees restricts the maximum sizes for high quality sawn timber. Timber products with dimensions exceeding this natural limit are examples of *Engineered wood products*, where timber boards are held together with adhesive, screws or nails. CLT panels are one of the latest additions to the engineered wood products. The creation of any CLT panels starts with the formation of each individual board, as each board is sawed, dried and graded into strength classes. Adhesive is then applied to the relevant sides of each board as the layers that constitute the sheet are formed. Compression through vacuum or hydraulics helps to keep the boards in place as the adhesive hardens [2].

An added benefit of the engineered wood products process is the homogenization of these products. In comparison to solid wood products, engineered wood product commonly exhibit far less variation in mechanical properties such as stiffness and strength [16, 19]. As the adhesive hardens, the panel can be bent to create different forms of curvature if the customer desires it. The possible arc of the panel is determined by the dimensions, especially thickness, of the panel, and its intended use [19].

The manufacturing process for CLT panels allows for immense dimensional freedoms. The maximum size of the panels is usually limited by the dimensional capability of the manufacturing facility. The thickness of the panels may vary between 60 and 500 mm, with a width between 0.8 and 4.8 m, and panels of lengths up to 30 m are available [2].

2.3 Finger joints

The natural anomalies and defects of wood creates a problem for the creation of longer timber boards. Cracks, knots and shakes limit the length of these timber boards and necessitates the usage of finger joints to join two or more boards for certain length spans. The finger joints are two interlocking sides profiled in such a way to achieve maximum contact area for the adhesive to efficiently join the two boards. As the boards are put together and the adhesive cures, the two timber boards now function much like a single board [1, 3]. Yet, finger joints are often regarded as weak points and a common source of failure for glued laminated timber beams subject bending. Weak points due to the presence of small voids between the fingerjoints, and also the thickness of the lamination, renders the material far more brittle [16].

2.4 Sustainability

Unlike other common building materials, such as steel, plastic or concrete, wood based products are organic and thus biodegradable. The recycling or re-usage of most non organic materials requires many costly steps, resulting in large deposits or landfills with negative environmental impact. Wooden products are easily recycled into energy, each kilo of dried wood containing 4.5 kWh, allowing more energy to be retained from recycling an average house with a wooden frame than it takes to construct the same house [20].

A European research project evaluated the average carbon emissions during the production phase for a four storey building complex. The results show little difference between the various wooden options, yet the carbon emission from options based on concrete were about 80 % higher than that of the average wooden construction [2].

For any country with a large forest industry, the increase in demand of wood based products will help to economically stimulate these industries, ensuring increased production and sufficient revenue for the industry to attain long term economic sustainability [21]. Having the material produced and manufactured in the same country also results in less transport distance and therefore less carbon emissions than importing non-native forms of material [2].

3 Material properties of wood

Wood, just like most organic materials, is intrinsically complex and properties may vary heavily between different species. It is thus necessary to understand the properties of wood from different perspectives, both the large scale macro-perspective along with the small micro- and sub-micro perspective.

3.1 Anatomy

Figure 3.1 gives an idealised illustration of a timber cross-section, labelling the different parts from a macro–perspective. Intrinsically complex, the inhomogeneous composition of wood necessitates a good understanding of the structure, its properties and parts if one is to adequately describe its mechanical behaviour. The inner heartwood consist of dead cells which, as long as outer sapwood still remains, will not decay nor lose any of its initial strength. The outer sapwood acts as the nutrient conduit for the tree, supplying the leaves with water for the process of photosynthesis, which in exchange produces a form of sugar called glucose. The sugar is dissolved in water and forms a viscous sap. The sap is carried from the leaves to the outer cambium and phloem layer where the sugary sap produces new sapwood and bark. What truly characterises the macro structure of a wood cross-section are the annual growth rings. The seasonal changes of temperate climates create yearly cyclical growth periods, where the lighter earlywood is formed during spring and early summer, while the darker rings, called latewood, are formed during the later parts of the summer. For further reading see [4, 22].

Every tree expands yearly in an approximately circular fashion, as illustrated in Figure 3.1. The annuals circular rings are used as a reference point to define the principal directions for the material:

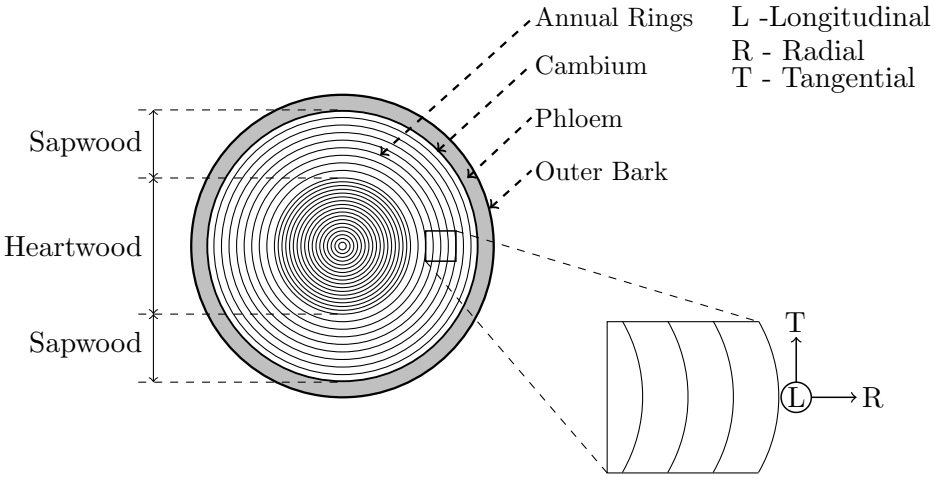

Figure 3.1: Idealised cross-section of a soft wood tree.

- **Longitudinal**: Runs approximately along the height of the tree trunk.
- **Radial**: Runs perpendicular to the annual rings, and is the normal to the annual rings.
- **Tangential**: Runs perpendicular to the radial direction, in the tangential direction of the annual rings.

The wood fibres run parallel to the longitudinal direction, and it is in the fibre direction wood exhibits the highest material strength and stiffness. The longitudinal elastic modulus typically being 10 to 20 times larger than the radial elastic modulus, while the tangential elastics modulus is at times double that of the radial. The varying properties in different directions orthogonal to one another is the definition of an orthotropic material [10, 13].

3.1.1 Micro scale

The micro scale is concerned with the behaviour of wood at a the level of the fibre cells. The cells are structured as long hollow tubes that run along the longitudinal axis of the tree, forming transport canals by which fluids are transported from the roots to the leaves. Softwood is composed of two types of fibre cells:

- **The tracheids**: Formed during the early growth season, the tracheids make up around 95% of all the cells in the tree, and provides most of the trees structural support.
- **The parenchyma**: Formed during the later part of the growth season, acting as carbon dioxide storage cells.

Since the tracheid cells are formed during the early growth period, characterised by considerable fluid transport and growth, these cells are far more voluminous than the parenchyma cells able to supply the tree with a larger abundance of nutrients. This difference in cellular vacancy translates into a drastic change in dry density, as the bulk density of the cellular wall usually ranges around 1500 kg/m^3 [13]. Along with the parenchyma and tracheid cells, there exist much larger fusiform cellular vessels that also help to transfer nutrients dissolved in water through the tree. These forms of transport tissues are referred to as *xylem*, the essential water conducting tissue of any vascular plants, i.e. plants with vertical upward water transportation [5]. The cellular wall consist of three primary substances; cellulose, hemicellulose and lignin.

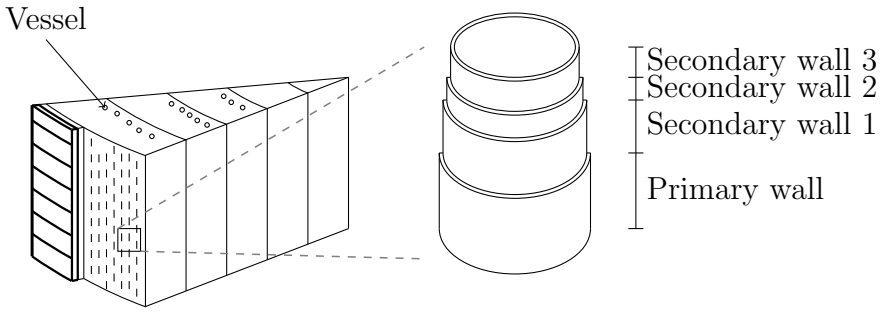

Figure 3.2: Illustration of a fibre cell and the cellular wall.

These are long polysaccharide chains formed by interconnecting the monosaccharide glucose into the micro fibrils that make up the cell walls. The different parts of the cell walls are labelled according to Figure 3.2. It is important to differentiate between the various layers of the cellular wall, since the distribution of the cellulose, hemicellulose and lignin varies considerably between the different layers, resulting in separate mechanical properties.

3.1.2 Anomalies

Figure 3.1 illustrates an idealised cross-section of a tree. In reality, no tree grows perfectly in accordance with the three principal orthotropic directions. Therefore, missalignment between the fibre direction and the three principal directions may result in lower durability and reduced strength properties. This is an important difference, since the mechanical properties of wood are usually described with the fibre direction as a reference. As has been mentioned previously, the material strength may vary substantially between these directions. This creates a potential problem from the growth of branches as they curve the fibre direction, running parallel to the branches instead of the stem [4, 13].

As the timber boards are formed and sawed, the branches will give rise to sound knots, a roughly cylindrical or conical shape curvature running parallel to the branch direction. If the branch has ceased to function and died, the remaining dead knot will instead form a much darker circle. These knots have large impact on the mechanical behaviour of timber, as they disturb the fibre direction, severely impacting the strength of the material. These natural anomalies will, depending on size, result in a lowered grading classification during testing [9].

3.2 Orthotropic behaviour

The relationship between stress and strain is called the constitutive relationship. For linear elastic behaviour, the relationship can be described by *Hooke's generalized law* in three dimensions [12]:

$$\sigma_i = D_{ij}\varepsilon_i; \quad \varepsilon_i = C_{ij}\sigma_i; \quad D_{ij}^{-1} = C_{ij} \text{ where : } \begin{array}{c|l} \sigma_i & \text{Stress vector} \\ D_{ij} & \text{The constitutive matrix} \\ \varepsilon_i & \text{Strain vector} \\ C_{ij} & \text{Flexibility matrix} \end{array}$$

$$\sigma_i = \begin{bmatrix} \sigma_{xx} \\ \sigma_{yy} \\ \sigma_{zz} \\ \tau_{xy} \\ \tau_{xz} \\ \tau_{yz} \end{bmatrix}; \quad D_{ij} = \begin{bmatrix} D_{11} & D_{12} & D_{13} & \cdots & D_{1j} \\ D_{21} & D_{22} & D_{23} & \cdots & D_{2j} \\ D_{31} & D_{32} & D_{33} & \cdots & D_{3j} \\ \vdots & \vdots & \vdots & \ddots & \vdots \\ D_{i1} & D_{i2} & D_{i3} & \cdots & D_{ij} \end{bmatrix}; \quad \varepsilon_i = \begin{bmatrix} \varepsilon_{xx} \\ \varepsilon_{yy} \\ \varepsilon_{zz} \\ \gamma_{xy} \\ \gamma_{xz} \\ \gamma_{yz} \end{bmatrix}; \quad \begin{array}{l} \gamma_{xy}{=}2{\cdot}\varepsilon_{xy} \\ \gamma_{xz}{=}2{\cdot}\varepsilon_{xz} \\ \gamma_{yz}{=}2{\cdot}\varepsilon_{yz} \end{array}$$

Orthotropic materials are a subset of anisotropic materials. Anisotropic materials, unlike isotropic materials, have varying material properties in different material dir-

ection and have no form of material symmetry. Orthotropic materials instead have three symmetry planes, reducing the amount of individual coefficients needed in the constitutive matrix to adequately describe the material behaviour. For an orthotropic material such as wood, the symmetry planes run parallel to the three principal directions of longitudinal, radial and tangential, described in Section 3.1. Hooke's generalised law for wood can be formulated as [16]:

$$\underbrace{\begin{bmatrix} \varepsilon_{LL} \\ \varepsilon_{RR} \\ \varepsilon_{TT} \\ \gamma_{LR} \\ \gamma_{LT} \\ \gamma_{RT} \end{bmatrix}}_{\varepsilon_i} = \underbrace{\begin{bmatrix} \frac{1}{E_L} & -\frac{\nu_{RL}}{E_R} & -\frac{\nu_{TL}}{E_T} & 0 & 0 & 0 \\ -\frac{\nu_{LR}}{E_L} & \frac{1}{\nu_R} & -\frac{\nu_{TR}}{E_T} & 0 & 0 & 0 \\ -\frac{\nu_{LT}}{E_L} & -\frac{\nu_{RT}}{E_R} & \frac{1}{E_T} & 0 & 0 & 0 \\ 0 & 0 & 0 & \frac{1}{G_{LR}} & 0 & 0 \\ 0 & 0 & 0 & 0 & \frac{1}{G_{LT}} & 0 \\ 0 & 0 & 0 & 0 & 0 & \frac{1}{G_{RT}} \end{bmatrix}}_{C_{ij}} \underbrace{\begin{bmatrix} \sigma_{LL} \\ \sigma_{RR} \\ \sigma_{TT} \\ \tau_{LR} \\ \tau_{LT} \\ \tau_{RT} \end{bmatrix}}_{\sigma_i}$$

Where E_L, E_R and E_T are the elastic modulus in the longitudinal, radial and tangential direction. The shear modulus G describes the ratio between the shear stress τ and shear strains γ. The coefficient ν denotes Poisson's ratio, describing the negative ratio between transverse and axial strain at uniaxial loading.

4 Structural dynamics

This chapter presents the theoretical background in structural dynamic and evaluation of metrics considered in the dissertation.

4.1 Equation of motion

To describe the equation of motion, there exists a necessity to understand the essential definitions and parameters affecting an arbitrary body. A force vector, described in Figure 4.1 as $d\mathbf{P}$, affecting an infinitesimally small surface area $d\mathbf{A}$, or $d\mathbf{S}$, is termed a traction vector if the infinitesimal area approaches zero. The vector n_i is a direction vector acting orthogonal to the body surface, while b_i describes the body force [12].

$$t_i = \begin{bmatrix} t_x \\ t_y \\ t_z \end{bmatrix} = \sigma_{ji} n_i = \begin{bmatrix} \sigma_{xx} n_x + \sigma_{xy} n_y + \sigma_{xz} n_z \\ \sigma_{yx} n_x + \sigma_{yy} n_y + \sigma_{yz} n_z \\ \sigma_{zx} n_x + \sigma_{zy} n_y + \sigma_{zz} n_z \end{bmatrix} ; \quad n_i = \begin{bmatrix} n_x \\ n_y \\ n_z \end{bmatrix} ; \quad b_i = \begin{bmatrix} b_x \\ b_y \\ b_z \end{bmatrix}$$

4.1.1 Strong formulation

For the strong formulation of the equation of motion, an arbitrary part of a body is selected. The body is subjected to two forces, its own body force and the traction force acting along the body surface described previously [15]. Formulated as Newtons second law in Eq. 4.1.1:

$$\int_S t_i dS + \int_V b_i dV = \int_V \rho \ddot{u}_i \, d\mathbf{V}; \qquad \text{(Eq. 4.1.1)}$$

As the expression is formulated in terms of both the body surface and area, the Gauss divergence theorem can help to reformulate the traction force in terms of the body

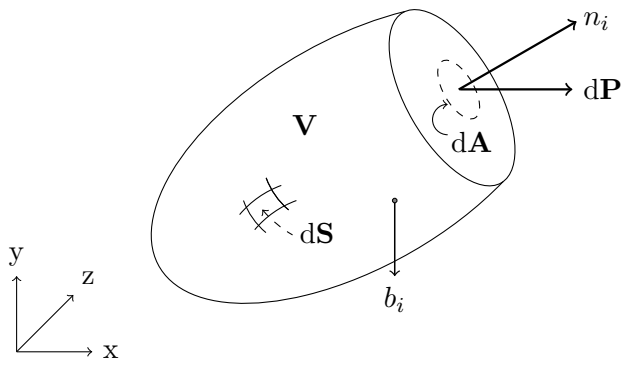

Figure 4.1: A visualisation of forces acting on a body.

volume. The Gauss divergence theorem state that:

$$\int_V q_{i,i}\, d\mathbf{V} = \int_S q_i n_i\, d\mathbf{S} \qquad \text{(Eq. 4.1.2)}$$

The traction force acting upon the arbitrary body's surface can through Eq. 4.1.2, and the definition given in the beginning of Section 4.1, be defined as:

$$\int_S \sigma_{ij} n_j\, d\mathbf{S} = \int_V \sigma_{ij,j}\, d\mathbf{V}$$

The initial equation of Eq. 4.1.1 is now solely described in terms of the body volume:

$$\int_V \left(\sigma_{ij,j} + b_i - \rho\ddot{u}_i\right)\, d\mathbf{V} = 0 \qquad \text{(Eq. 4.1.3)}$$

The equation now holds for any volume V, and the strong formulation is given in Eq. 4.1.4 as:

$$\sigma_{ij,j} + b_i = \rho\ddot{u}_i \qquad \text{(Eq. 4.1.4)}$$

4.1.2 Weak formulation

To move from the strong formulation to the weak formulation, Eq. 4.1.4 is multiplied by a weight function v_i, representing virtual displacement, and integrated over the arbitrary body:

$$\int_V v_i \left(\sigma_{ij,j} + b_i - \rho\ddot{u}_i\right)\, d\mathbf{V} = 0 \qquad \text{(Eq. 4.1.5)}$$

Using the relationship derived from the Green Gauss theorem:

$$\int_V (\phi_i\psi_{ij,j} + \phi_{i,j}\psi_{ij}) d\mathbf{V} = \int_V (\phi_i\psi_{ij})_{,j}\, d\mathbf{V} \qquad \text{(Eq. 4.1.6)}$$

Defining the variable $\phi_i = v_i$ and $\psi_{ij} = \sigma_{ij}$ in Eq. 4.1.6:

$$\int_V (v_i\sigma_{ij,j} + v_{i,j}\sigma_{ij}) d\mathbf{V} = \int_V (v_i\sigma_{ij})_{,j}\, d\mathbf{V} \qquad \text{(Eq. 4.1.7)}$$

Inserted into Eq. 4.1.5:

$$\int_V (v_i\sigma_{ij})_{,j} d\mathbf{V} - \int_V v_{i,j}\sigma_{ij} d\mathbf{V} + \int_V v_i b_i d\mathbf{V} = \int_V \rho\ddot{u}_i\, d\mathbf{V} \qquad \text{(Eq. 4.1.8)}$$

Using Gauss divergence theorem in Eq. 4.1.6, the first term in eq Eq. 4.1.2 can be redefined in terms of the arbitrary body's surface, resulting in the weak formulation:

$$\int_V \rho v_i\ddot{u}_i\, d\mathbf{V} + \int_V v_{i,j}\sigma_{ij} d\mathbf{V} = \int_S v_i t_i d\mathbf{S} + \int_V v_i b_i d\mathbf{V} \qquad \text{(Eq. 4.1.9)}$$

4.2 Finite element method

The finite element method is a numerical method used to solve complex partial differential equations, characterised by having initial- and boundary conditions. The

fundamental principle is the division of domains into smaller subdomains, elements, where the global behaviour is described through local approximation functions over each subdomain.

Within the ABAQUS library there exists a wide range of elements, depending on the problems at hand. 3D continuum elements are commonly formed as either tetrahedrons, solid bricks, or triangular elements constructed using a certain number of nodes, depending on quadratic or linear interpolation. Each node has three degrees of freedom representing the displacements in the three spatial directions, see figure 4.2. 3D solid continuum elements are commonly used to solve stress and displacement problems [17].

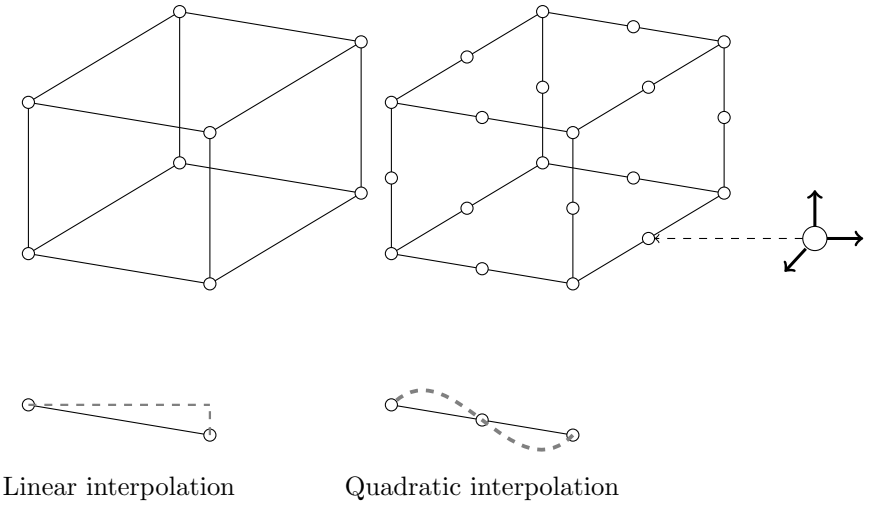

Figure 4.2: Visual illustration of the difference between first and second order elements

Quadratic and linear elements refer to the means of calculating the displacement existing between two corner nodes. Linear interpolation assumes the displacement between two points to be described as linear. An element using linear interpolation is referred to as a first order element. The quadratic, or second order element assumes that the displacement variation along the edge may be defined as having a quadratic variation, which is why there is a third node added to the edge between two corner nodes, see Figure 4.2. Second order elements are considered to be far more accurate than first order elements when dealing with problem not including complex contact conditions or severe element distortion. Instead, second order elements are ideal when dealing with bending dominated problems.

4.2.1 FE-formulation of motion

In the FE-method, the behaviour of the body is described through approximation functions. The displacement u is approximated by the global time–independent shape function N and the nodal displacement by the vector a.

$$u = Na \Rightarrow \dot{u} = N\dot{a}\,;\ \ddot{u} = N\ddot{a}$$

Using the Galerkin method the following arbitrary functions and vectors are chosen:

$$v_i = N_i c_i\,;\ \ v_i^T = N_i^T c_i^T\,;\ \ v_{i,j} = B_{ij} c_i\,;\ \ B_{ij} = N_{i,j}$$

The input variables are now described in accordance with the formulation from the constitutive relationship in Section 3.2:

$$\sigma_i^T = \begin{bmatrix} \sigma_{xx} & \sigma_{yy} & \sigma_{zz} & \sigma_{xy} & \sigma_{xz} & \sigma_{yz} \end{bmatrix}; \qquad \sigma_i = D_{ij}\varepsilon_i = D_{ij}B_{ij}a_i$$

Inserted into the weak formulation:

$$c_i^T \left(\int_V B_{ij}^T \sigma_i d\mathbf{V} - \int_S N_i^T t_i d\mathbf{S} - \int_V N_i^T b_i d\mathbf{V} + (\int_V \rho N_i^T N_i d\mathbf{V})\ddot{a}_i \right) = 0$$

The equilibrium equation can now be solved independent of the arbitrary weight vector c_i. The complete FE-formulation of the equation of motion is deduced to:

$$\underbrace{\int_V B_{ij}^T D_{ij} B_{ij}}_{K_{ij}} a_i d\mathbf{V} + \underbrace{(\int_V \rho N_i^T N_i d\mathbf{V})}_{M_{ij}} \ddot{a}_i = \underbrace{\int_S N_i^T t_i d\mathbf{S} - \int_V N_i^T b_i d\mathbf{V}}_{f_i} \qquad \text{(Eq. 4.2.1)}$$

To give the formulation a better appearance, the system is reduced to:

$$M_{ij}\ddot{a}_i + K_{ij}a_i = f_i \qquad \text{(Eq. 4.2.2)}$$

The equation can also be written in matrix form as:

$$\mathbf{M\ddot{a}} + \mathbf{Ka} = \mathbf{f}$$

4.3 Calculation of eigenmodes

Free vibration of a system is the dynamic response of a structure disturbed from its equilibrium position, i.e. not subject to any external forces or dynamic excitation. A multiple degree of freedom system without damping is defined as:

$$\mathbf{M\ddot{u}}(t) + \mathbf{Ku}(t) = 0; \qquad \text{where:} \quad \begin{array}{c|l} \mathbf{M} & \text{Mass matrix} \\ \mathbf{K} & \text{Stiffness matrix} \\ \mathbf{u} & \text{Deformation} \\ \mathbf{\ddot{u}} & \text{Acceleration} \end{array}$$

The displacement of the free vibrations system is described as being a harmonic time dependent function, given the form:

$$\mathbf{u}(t) = \phi_n \underbrace{(A_n\, cos(\omega_n t) + B_n\, sin(\omega_n t))}_{q_n(t)} = \phi_n q_n(t) \qquad \text{(Eq. 4.3.1)}$$

$$T_n = \frac{2\pi}{\omega_n}; \quad f_n = \frac{1}{T_n}; \quad \text{where :} \quad \begin{array}{c|l} T_n & \text{n:th natural period [s]} \\ f_n & \text{n:th natural frequency [Hz]} \\ \omega_n & \text{n:th natural frequency [rads/s]} \end{array}$$

$\phi_n = [\phi_{1n} \quad \phi_{2n} ...]^T$ being the natural modes for the undamped structure and the deformation having the following derivatives:

$$\dot{\mathbf{u}}(t) = \phi_n \omega_n (-A_n\, sin(\omega_n t) + B_n\, cos(\omega_n t))$$

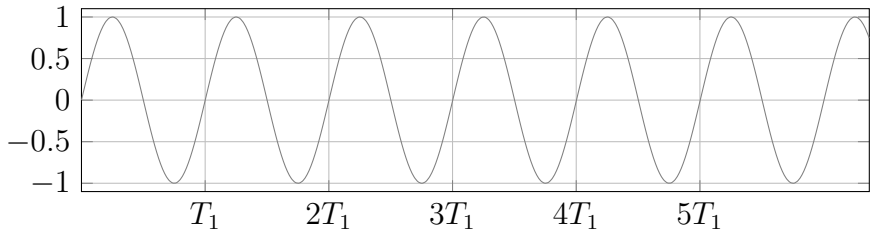

Figure 4.3: Free vibration of an undamped system.

$$\ddot{\mathbf{u}}(t) = -\phi_n \omega_n^2 (A_n \, cos(\omega_n t) + B_n \, sin(\omega_n t))$$

By substituting Eq. 4.3.1 into the equation for a free system without damping, defined previously, the following equation is acquired:

$$\left[-\mathbf{M}\omega_n^2 \phi_n + \mathbf{K}\phi_n\right] q_n(t) = \mathbf{0} \qquad \text{(Eq. 4.3.2)}$$

The equation has an initial trivial solution when the deformation $\mathbf{u}(t) = 0$ and there exists no motion within the system. But, the system also has a formal solution in Eq. 4.3.2, solved through the vector ϕ_n and the modal natural frequency ω_n as:

$$[-\omega_n^2 \mathbf{M} + \mathbf{K}]\phi_n = \mathbf{0} \qquad \text{(Eq. 4.3.3)}$$

This equation also has a trivial solution when the system is not in motion as $\phi_n = 0$ and a nontrivial solution:

$$\det\left(-\omega_n^2 \begin{bmatrix} m_{11} & \cdots & m_{1n} \\ \vdots & \ddots & \vdots \\ m_{n1} & \cdots & m_{nn} \end{bmatrix} + \begin{bmatrix} k_{11} & \cdots & k_{1n} \\ \vdots & \ddots & \vdots \\ k_{n1} & \cdots & k_{nn} \end{bmatrix}\right) = 0$$

The equation has the same amount of positive roots as there exist degrees of freedom for the system. As the characteristic equation is solved and the natural frequencies ω_n are determined, Eq. 4.3.3 may be solved for the corresponding modal vector ϕ_n.

$$\Phi_{ij} = [\phi_{in}] = \begin{bmatrix} \phi_{11} & \phi_{12} & \cdots & \phi_{1n} \\ \phi_{21} & \phi_{22} & \cdots & \phi_{2n} \\ \vdots & \vdots & \ddots & \vdots \\ \phi_{i1} & \phi_{i2} & \cdots & \phi_{in} \end{bmatrix}; \quad \text{where :} \quad \begin{array}{c|l} \Phi_{ij} & \text{Modal matrix} \\ i & \text{Corresponding DOF} \\ n & \text{Corresponding eigenvector} \end{array}$$

4.4 Classically damped system

For structures consisting of parts with similar damping mechanisms, classical forms of damping are usually considered. For a classically damped system the damping is idealised in a damping matrix. Rayleigh damping is a form of classical damping where the damping of a structure is assumed to originate from both the mass and stiffness of the structure. Stiffness proportional damping is due to the energy dissipation in structures from deformations and is related to the coefficient a_1 in:

$$C_n = a_1 \omega_n^2 M_n; \quad \zeta_n = \frac{a_1}{2}\omega_n; \quad \text{where :} \quad \begin{array}{c|l} C_n & \text{Generalized damping n:th mode} \\ M_n & \text{Generalized mass n:th mode} \\ \zeta_n & \text{Damping ratio for n:th mode} \end{array}$$

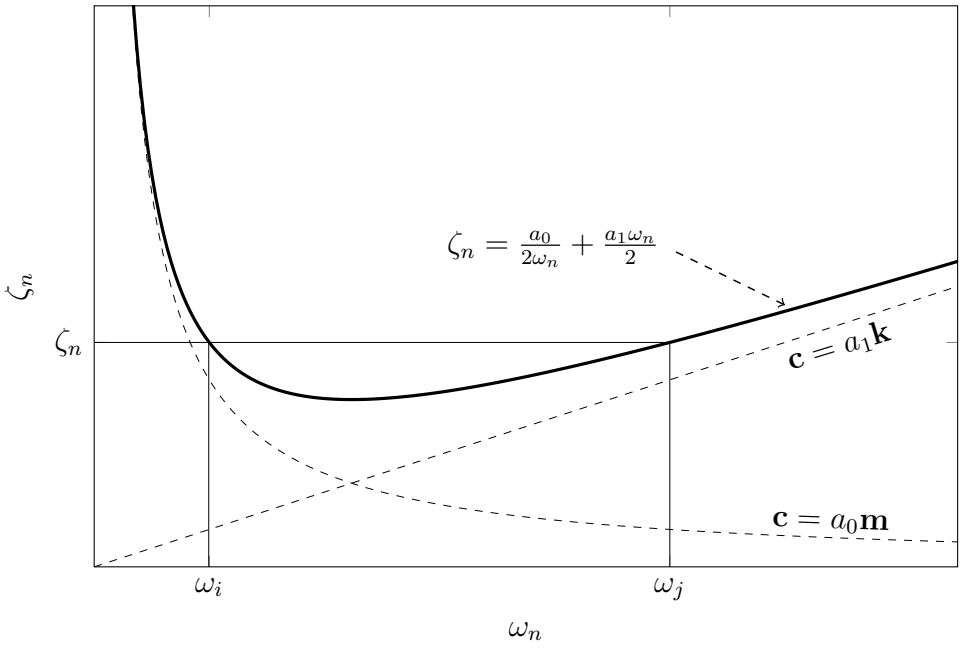

Figure 4.4: Rayleigh damping model determining the damping ratio, ζ_n, using the mass and stiffness proportional damping coefficients for a frequency interval ω_i – ω_j.

The mass proportional damping is related to the coefficient a_0 and defined in:

$$C_n = a_0 M_n; \quad \zeta_n = \frac{a_0}{2\omega_n} \qquad \text{(Eq. 4.4.1)}$$

The Rayleigh damping is defined in terms of both the mass- and stiffness proportional damping as:

$$\mathbf{C} = a_0\mathbf{M} + a_1\mathbf{K} \qquad \text{(Eq. 4.4.2)}$$

With the damping ratio ζ_n, for the n:th mode, being described as:

$$\zeta_n = \frac{a_0}{2\omega_n} + \frac{a_1\omega_n}{2}$$

For two modes assumed or determined to have the same damping ratio the two coefficients a_0 and a_1 can individually be solved through:

$$a_0 = \zeta\frac{2\omega_i\omega_j}{\omega_i + \omega_j}; \quad a_1 = \zeta\frac{2}{\omega_i + \omega_j}$$

4.5 Modal analysis of classically damped systems

For any MDOF system with n known natural modes the displacement vector can be described through modal expansion. This allows for the displacement to be described in terms of modal contribution as:

$$\mathbf{u} = \sum_{i=1}^{n} \phi_i q_i = \mathbf{\Phi q}\,; \quad \text{Where:} \quad \begin{array}{l|l} q_i & i\text{:th modal cordinate} \\ \phi_i & i\text{:th eigen mode} \end{array}$$

Consider the MDOF system with damping subject to a harmonic force in Eq. 4.5.1:

$$\mathbf{M}\ddot{\mathbf{u}} + \mathbf{C}\dot{\mathbf{u}} + \mathbf{K}\mathbf{u} = \mathbf{P}(t) \qquad \text{(Eq. 4.5.1)}$$

Using modal expansion described previously, the system displacements may be rewritten in terms of modal contribution as:

$$\sum_{i=1}^{n} \mathbf{M}\phi_i \ddot{q}_i(t) + \sum_{i=1}^{n} \mathbf{C}\phi_i \dot{q}_i(t) + \sum_{i=1}^{n} \mathbf{K}\phi_i q_i(t) = \mathbf{P}(t) \qquad \text{(Eq. 4.5.2)}$$

Multiplying all terms in Eq. 4.5.2 with ϕ_n^T:

$$\sum_{i=1}^{n} \phi_n^T\mathbf{M}\phi_i \ddot{q}_i(t) + \sum_{i=1}^{n} \phi_n^T\mathbf{C}\phi_i \dot{q}_i(t) + \sum_{i=1}^{n} \phi_n^T\mathbf{K}\phi_i q_i(t) = \phi_n^T\mathbf{P}(t) \qquad \text{(Eq. 4.5.3)}$$

Due to the orthogonality of natural modes which dictates that:

$$\text{if} \begin{cases} i \neq n: & \phi_n^T\mathbf{K}\phi_i = 0\ ; & \phi_n^T\mathbf{M}\phi_i = 0; & \phi_n^T\mathbf{C}\phi_i = 0 \\ i = n: & \phi_n^T\mathbf{K}\phi_i = K_n\ ; & \phi_n^T\mathbf{M}\phi_i = M_n; & \phi_n^T\mathbf{C}\phi_i = C_n \end{cases}$$

All the terms in each summation disappear except those fulfilling the criteria of modal orthogonality i.e. When i=n, the system in Eq. 4.5.1 is rewritten as:

$$M_n\ddot{q}_n(t) + C_n\dot{q}_n(t) + K_n q_n(t) = P_n(t) \qquad \text{(Eq. 4.5.4)}$$

Where:	M_n	Generalised mass n:th mode
	C_n	Generalised damping n:th mode
	K_n	Generalised stiffness n:th mode
	P_n	Generalised force n:th mode

Eq. 4.5.4 may be regarded as the governing equation of a SDOF system for the n:th natural mode. Therefore, a MDOF with N natural modes may be written as a set of equations in matrix form accordingly:

$$\mathbf{M}\ddot{\mathbf{q}} + \mathbf{C}\dot{\mathbf{q}} + \mathbf{K}\mathbf{q} = \mathbf{P}(t) \qquad \text{(Eq. 4.5.5)}$$

Where:

$$\mathbf{M}= \begin{bmatrix} M_1 & & & \\ & M_2 & & \\ & & \ddots & \\ & & & M_N \end{bmatrix};\ \mathbf{C}= \begin{bmatrix} C_1 & & & \\ & C_2 & & \\ & & \ddots & \\ & & & C_N \end{bmatrix}$$

$$\mathbf{K}= \begin{bmatrix} K_1 & & & \\ & K_2 & & \\ & & \ddots & \\ & & & K_N \end{bmatrix};\ \mathbf{P}= \begin{bmatrix} P_1(t) & & & \\ & P_2(t) & & \\ & & \ddots & \\ & & & P_N(t) \end{bmatrix}$$

The resulting displacement for the system is determined by combining the modal contributions as:

$$\mathbf{u}(t) = \sum_{i=1}^{N} \phi_i q_i(t) \qquad \text{(Eq. 4.5.6)}$$

4.6 Steady state dynamic analysis

The steady state analysis provides the dynamic steady state response of a system subject to harmonic excitation at a given frequency. The analysis is usually performed as a frequency sweep divided into a set number of increments. For each incremental increase the dynamic response is calculated and saved. Therefore, a steady state analysis using a large number of iterations for a numerically complex model may necessitate considerable computing power.

Two common approaches for accessing the steady-state response of a system are the direct-solution and mode-based approach. The direct-solution steady-state analysis considers the system in terms of the individual degrees of freedom for the whole model, resulting in a accurate yet computationally expensive analysis. The mode-based steady-state use the principle of modal superposition described in Section 4.5. This allows the system to be described using a set of diagonalised matrices, resulting in less accurate but computationally cheaper and less time consuming steady-state analysis. A problem for the mode-based approach is discerning the amount of eigenmodes to use to adequately model the dynamic response of the system, as increasing the amount of eigenmodes for the steady-state analysis results in larger sets of equation for the computer to solve.

4.7 Evaluation metrics

When performing comparative studies the means of calculating differences may vary between different fields of study. This section is concerned with describing metrics commonly used when comparing different models.

4.7.1 Root mean square

The root mean square function, or RMS, is defined as the square root of the sum of each individual sample point squared divided by the amount of sample points. The RMS value is a metric for estimating the response of a certain function.

$$\mathbf{RMS} = \sqrt{\frac{1}{n}\sum_{n} x_i^2}; \quad \text{where:} \quad \begin{array}{c|l} \text{n} & \text{Sample size} \\ x_i & \text{Value of the } i\text{:th sample point} \end{array}$$

4.7.2 Normalised relativ frequency difference

In order to study and compare the eigenfrequencies between different models, the normalised relative frequency difference (NRFD) is commonly used, calculated according to Eq. 4.7.1. Here f_i^r is the i:th eigenfrequency for the reference model and f_i^a is the corresponding eigenfrequency for the alternative model.

$$\text{NRFD} = \frac{|f_i^r - f_i^a|}{f_i^r} \qquad \text{(Eq. 4.7.1)}$$

4.7.3 Percentage error

The RMS percentage error is the relative difference between the RMS value for a reference model and the value of the alternative model in percent, calculated as:

$$\text{Error } [\%] = 100 \cdot \left| \frac{RMS_{Alternative} - RMS_{Reference}}{RMS_{Reference}} \right| \qquad \text{(Eq. 4.7.2)}$$

4.7.4 Velocity error

The velocity error is calculated as the non-weighted difference in error for a specific frequency. Described as the absolute value of the velocity difference for the reference model and the alternative model:

$$v_{error} = \left| v_{Reference} - v_{Alternative} \right| \qquad \text{(Eq. 4.7.3)}$$

5 Numerical models

The CLT panel has seven layers and the following dimensions: 2 m × 6.285 m × 0.245 m (Width × Length × Height). To determine a suitable numerical model to evaluate the dynamic analysis of a CLT panel, three different numerical models are compared. These are named the High-fidelity, Layered and Composite model. All models are constructed and evaluated in ABAQUS, employing different approaches to describe the orthogonal layering. The panel is considered to be simply supported, with the displacement boundary conditions acting horizontally along the middle of the cross-section. The displacement boundary conditions for one side is prescribed to zero, while the boundary conditions for the opposite side is prescribed to zero in the z and y-direction, see Figure 5.2. Deviations, such as fibre misalignment or finger joints, are assumed to be negligible for the analysis. The material parameters for the softwood is modelled according to the parameters for spruce of a C24 strength class, see Table 5.1.

Table 5.1: The material parameters used to describe C24 [7].

	E_L	E_R	E_T	G_{LR}	G_{LT}	G_{RT}	ν_{LR}	ν_{LT}	ν_{TR}	ρ
Dimension	MPa	MPa	MPa	MPa	MPa	MPa	-	-	-	kg/m^3
Spruce	11 000	370	370	690	690	50	0.51	0.38	0.31	420

5.1 High-fidelity 3D model

For the High-fidelity model each individual timber board along with the adhesive is taken into account. High-fidelity, in this case, denotes the high detail correspondence between the model and a CLT panel. Each individual board is modelled according to the ortotropic behaviour for wood, described in Section 3.2, where the longitudinal direction runs along the length of the board. The panel consists of seven layers, each layer being 35 mm and ordered orthogonally to the previous layer. In each layer the boards are arranged parallel with one another, separated horizontally by a thin 0.2 mm wide adhesive, the adhesive is modelled as a 0.2 mm wide void. The outer most boards have different dimensions than the dimensions given in Table 5.2, and are described in Figure 5.1.

The decision to model the gaps for the High-fidelity model separates its dynamic behaviour from the two other alternative models. For both the Layered and the Composite model, there is assumed to be full horizontal interaction between two parallel boards in a layer. The adhesive in the High-fidelity model limits the interaction between boards to only exist vertically, i.e. there exist no form of interaction between boards in the same layer. This results in the wave propagation through the High-fidelity model to move solely between boards vertically.

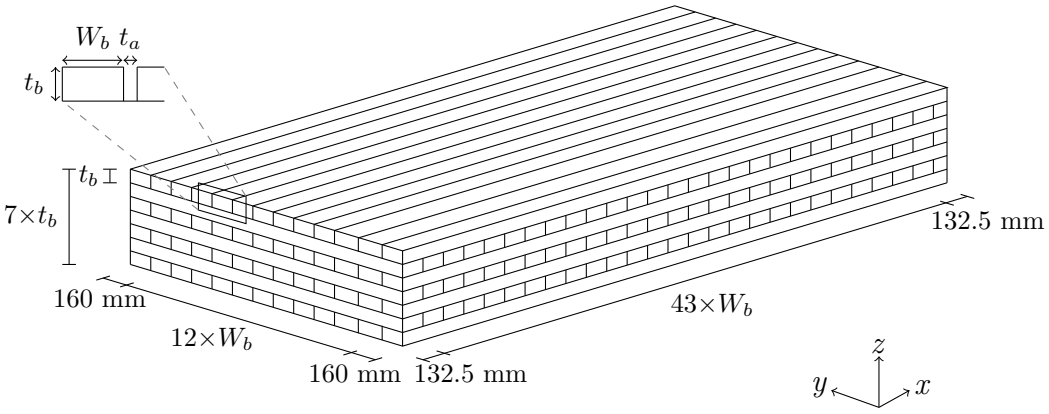

Figure 5.1: A visualisation of the High-fidelity 3D model with the dimensions described in Table 5.2. The outer boards have been assigned different dimensions to fit the dimensions of the CLT panel.

Table 5.2: The dimensions of the High-fidelity 3D model in Figure 5.2.

	Description	Symbol	Value	Dimension
High-fidelity 3D Model	Width	W	2 000	mm
	Length	L	6 285	mm
	Height	H	245	mm
Board	Board width	W_b	140	mm
	Board thickness	t_b	35	mm

Modelling the adhesive as a 0.2 mm void also impacts the mass matrix and the global stiffness matrix, since the void contributes nothing to either matrices. Differences in the stiffness and mass matrices will (see Eq. 4.3.3) also result in larger variations between eigenfrequencies when comparing two models. Consider also problems using Rayleigh damping, where the damping matrix is dependent on both the mass and stiffness matrices.

The High-fidelity model is created using quadratic solid 3D continuum brick blocks in ABAQUS, having a total of 20 nodes per element (C3D20). Engineering constants and material orientation are used to define the material parameters for each board in the three spacial directions. The maximum element length is restricted to 140 mm for all analysis.

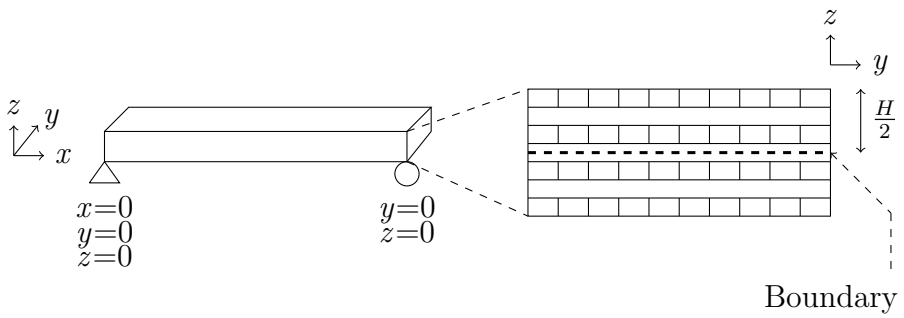

Figure 5.2: An illustration of the displacement boundary conditions applied over the cross section of the CLT panel.

5.2 Layered 3D model

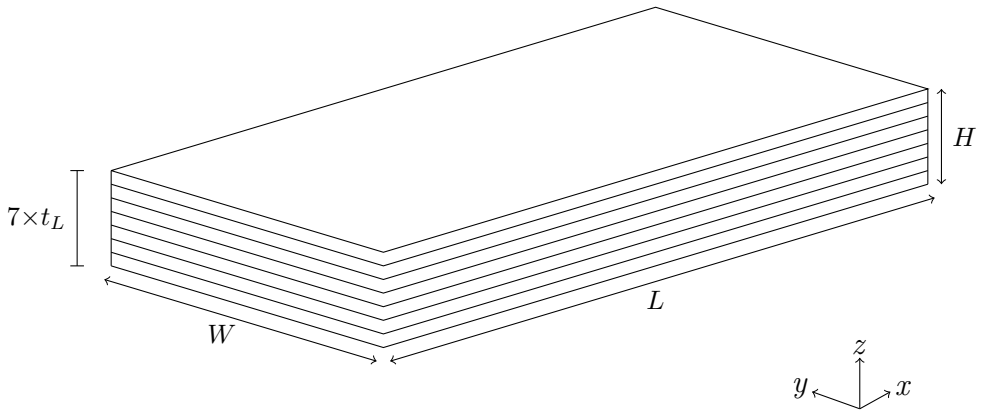

Figure 5.3: A visualisation of the Layered 3D model.

Table 5.3: The dimensions of the Layered 3D model visualised in Figure 5.3.

	Description	Symbol	Value	Dimension
Layered 3D model	Width	W	2 000	mm
	Length	L	6 285	mm
	Height	H	245	mm
Layer	thickness	t_L	35	mm

The Layered model consists of seven layers, each being 35 mm thick. Each layer is created as a solid, neglecting to model the boards individually and the gap separating them. This results in full interaction vertically between parallel layers, but also complete horizontal interaction between parallel boards within a layer, unlike the High fidelity model. Omitting to model the individual gaps will result in greater stiffness for the Layered model than the High-fidelity model, but also less elements. The reduced amount of elements needed for the Layered model results in a less complex system of equations and therefore less computational power nessecary for an analysis. The material orientation for each layer is ordered orthogonal to the previous, like the other models. Using quadratic 3D continuum brick elements with a maximum length of 140 mm (C3D20) in ABAQUS.

5.3 Composite 2D model

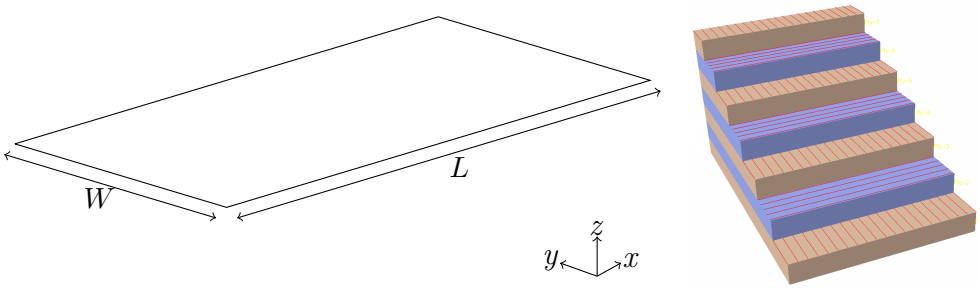

Figure 5.4: A visualisation of the Composite 2D model and the seven plies created in ABAQUS.

Table 5.4: The dimensions of the Composite 2D model.

	Description	Symbol	Value	Dimension
Composite 2D	Width	W	2 000	mm
	Length	L	6 285	mm

The Composite model is constructed using 2D six degree of freedom per node quadratic shell element, with a maximum length of 140 mm. The material properties and orthogonal behaviour for each layer are described using seven different plies in ABAQUS ply stack function, see Figure 5.4. The Composite model, just like the Layered model, omits the modelling of the gaps. Therefore there exists full interaction both vertically and horizontally between parallel layers and boards. The Composite model and the Layered model both consider the CLT-panels layers to be solids. Both models have the same panel dimension, but two different approaches to describe the orthogonal layering.

A problem with comparing a 2D model with a 3D model is the application of loads and boundary conditions at different vertical positions. For the 3D models the boundary conditions are applied in the middle of the cross-section while the loads are applied at the surface level, but, for the 2D model the boundary conditions and loads are projected on the 2D shell.

5.4 Validation of model

Validating the High-fidelity model is done by comparing the results from the eigenvalue analysis with the results of another numerical model. In a study from the University of New Brunswick, a numerical model of a CLT panel was created and verified by comparing the modal behaviour with experimental data from a laboratory built CLT panel. The comparison was made for eigenfrequencies below 100 Hz, both models having the corresponding dimensions of the High-fidelity model [23].

In Table 5.5 the eigenmodes below 100 Hz for the High-fidelity model and the numerical model from the study are compared. The relative error is described in terms of NRFD in Eq. 4.7.1. Although the two models have the same dimensions, the material properties differ. Therefore, the comparison is concerned with comparing the modal sequence of both models, and allows for some frequency difference between the two models. The aim is to ascertain corespondent modal behaviour for the two numerical models. From Table 5.5 both models exhibit the same modal sequence, with the largest NRFD existing for mode (1,2). The NRFD is larger for modes with half sine waves above one in the y-direction, i.e. mode (1,2) and (2,2).

Table 5.5: Comparison of eigenfrequencies between the High-fidelity 3D model and the alternative CLT model from the study in [23].

Mode	(1,1)	(1,2)	(2,1)	(2,2)	(3,1)
High-fidelity 3D model	11.5	19.6	39.6	48.2	74.8
Ussher et al [23]	11.5	22.9	39.1	51.8	72.7
NRFD [%]	0	16.8	1.3	7.5	2.8

6 Effect on dynamic properties

The dynamic properties chapter is concerned with comparing the eigenfrequencies and eigenmodes for the three models described in Chapter 5. The eigenvalue analysis is performed for frequencies below 120 Hz for the High-fidelity model. Any mode existing inside the frequency range for the High-fidelity model will be included for any other model, even if the mode is above 120 Hz. The eigenvalue analysis aims at comparing the modal behaviour of each model in comparison to the High-fidelity model, i.e. concluding what differences separate the different models in terms of dynamic properties, and ascertaining the validity of using either the Layered or the Composite model to adequately replicate the behaviour of the High-fidelity model.

6.1 High-fidelity 3D model

The eigenfrequencies and mode shapes of the High-fidelity model is determined using quadratic 3D continuum elements, modelling the gaps between each board in the same layer as 0.2 mm voids. The first eight numerically determined eigenmodes are illustrated in Figure 6.1, while the corresponding eigenfrequencies are given in Table 6.1.

The modes for the High-fidelity model do not include more than two half sine waves in the y-direction, see Figures 6.1–6.3. This means that only eigenmode two, four, six and eight exhibit bending and or twisting about the x-direction, while all eigenmodes display bending about the y-direction.

Table 6.1: Summary of the first eight eigenfrequencies for the High-fidelity 3D model.

Mode	(1,1)	(1,2)	(2,1)	(2,2)	(3,1)	(3,2)	(4,1)	(4,2)
Frequency [Hz]	11.47	19.62	39.60	48.24	74.81	82.81	112.21	119.67
Figure 6.1	(a)	(b)	(c)	(d)	(e)	(f)	(g)	(h)

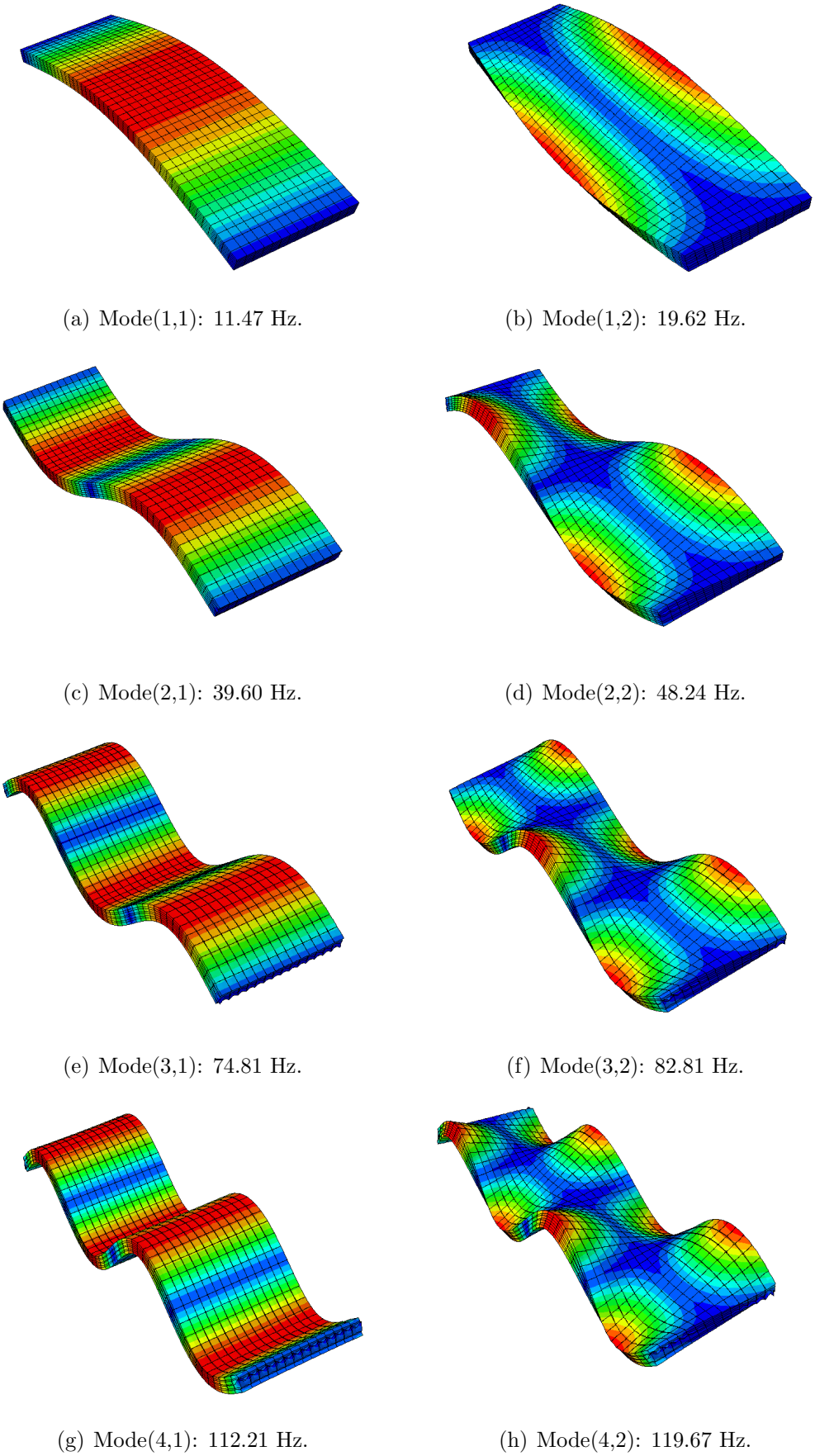

(a) Mode(1,1): 11.47 Hz.

(b) Mode(1,2): 19.62 Hz.

(c) Mode(2,1): 39.60 Hz.

(d) Mode(2,2): 48.24 Hz.

(e) Mode(3,1): 74.81 Hz.

(f) Mode(3,2): 82.81 Hz.

(g) Mode(4,1): 112.21 Hz.

(h) Mode(4,2): 119.67 Hz.

Figure 6.1: The first eight eigenmodes computed with the High-fidelity 3D model.

6.2 Layered 3D model

The Layered model is created using the same quadratic 3D continuum elements as the High-fidelity model. However, as has been mentioned in Section 5.1, the Layered model considers each layer to be a solid, omitting to model each individual board or gap separating them. The first eight numerically determined eigenmodes are illustrated in Figure 6.2, while the corresponding eigenfrequencies are given in Table 6.2.

The Layered model exhibit the same eigenmodes as the High-fidelity model and in the same order. The eigenfrequencies for the Layered model are marginally higher than those of the High-fidelity model, this being true for all eigenfrequencies.

Table 6.2: Summary of the first eight eigenfrequencies computed with the Layered 3D model.

Mode	(1,1)	(1,2)	(2,1)	(2,2)	(3,1)	(3,2)	(4,1)	(4,2)
Frequency [Hz]	11.53	22.45	39.93	52.21	75.62	87.33	113.65	124.70
Figure 6.2	(a)	(b)	(c)	(d)	(e)	(f)	(g)	(h)

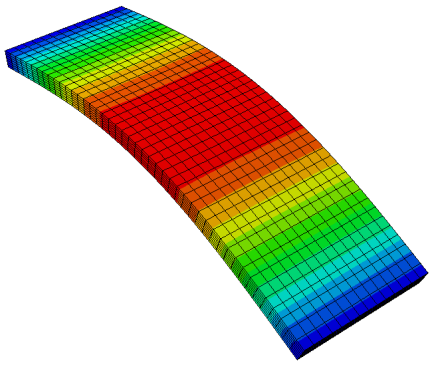

(a) Mode(1,1): 11.53 Hz.

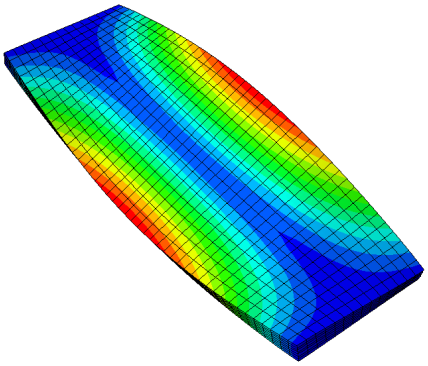

(b) Mode(1,2): 22.45 Hz.

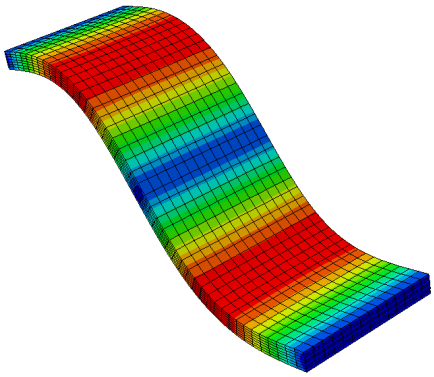

(c) Mode(2,1): 39.93 Hz.

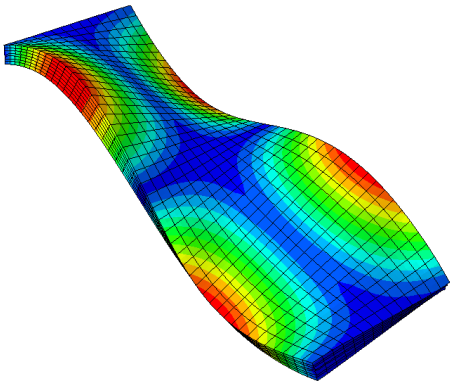

(d) Mode(2,2): 52.21 Hz.

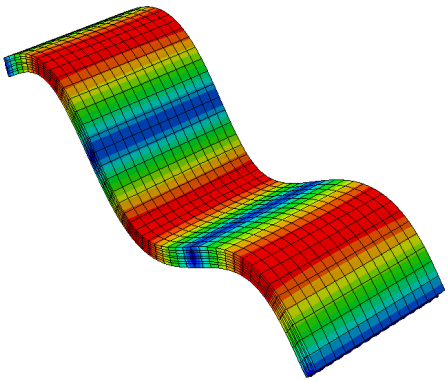

(e) Mode(3,1): 75.62 Hz.

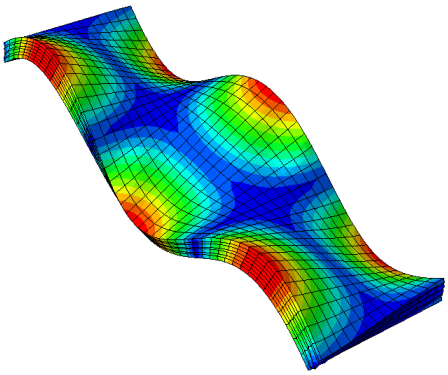

(f) Mode(3,2): 87.33 Hz.

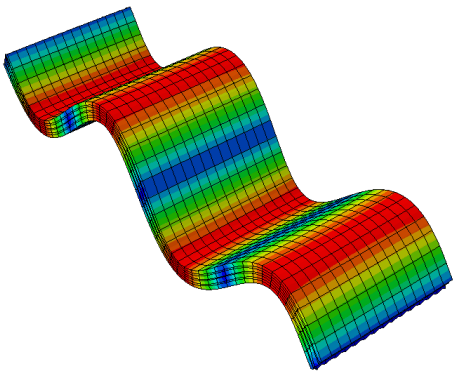

(g) Mode(4,1): 113.65 Hz.

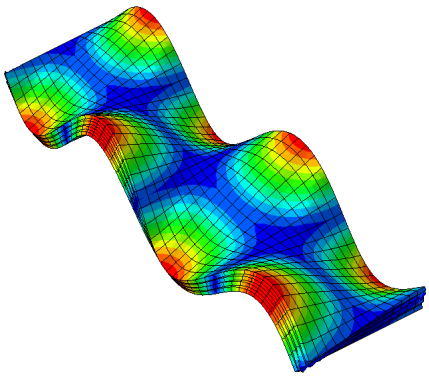

(h) Mode(4,2): 124.70 Hz.

Figure 6.2: The first eight eigenmodes of the Layered 3D model.

6.3 Composite 2D model

The Composite model is evaluated using 2D quadratic shell elements, modelling each layer as a solid, using the ply-stack function in ABAQUS. The first eight numerically determined eigenmodes for the Composite modell are illustrated in Figure 6.3, while the corresponding eigenfrequencies are given in Table 6.3.

The eigenfrequencies for the Composite model are marginally higher than those of the High-fidelity model, just like the Layered model. The modal sequence for the Composite model corresponds with both the Layered and the High-fidelity model for the first eight eigenmodes.

Table 6.3: Summary of the first eight eigenfrequencies computed with the Composite 2D model.

Mode	(1,1)	(1,2)	(2,1)	(2,2)	(3,1)	(3,2)	(4,1)	(4,2)
Frequency [Hz]	11.57	22.43	40.12	52.33	75.94	87.53	113.76	124.60
Figure 6.3	(a)	(b)	(c)	(d)	(e)	(f)	(g)	(h)

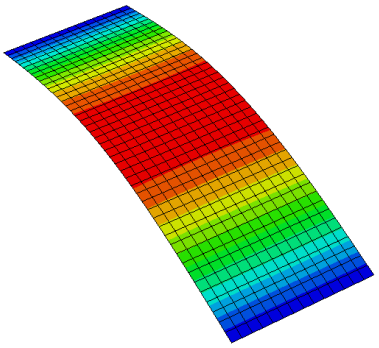

(a) Mode(1,1): 11.57 Hz.

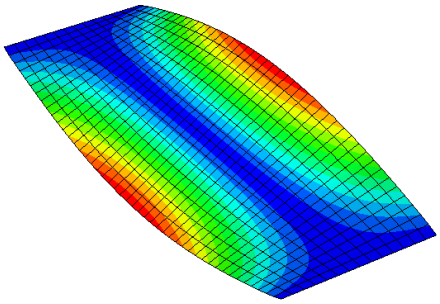

(b) Mode(1,2): 22.43 Hz.

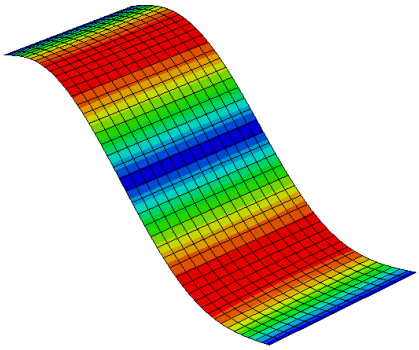

(c) Mode(2,1): 40.12 Hz.

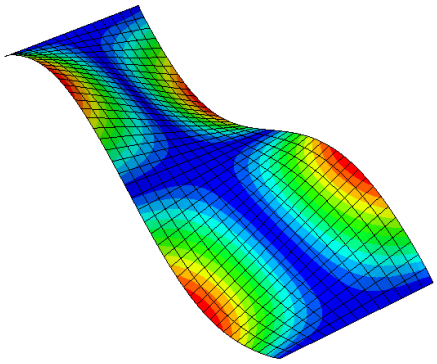

(d) Mode(2,2): 52.33 Hz.

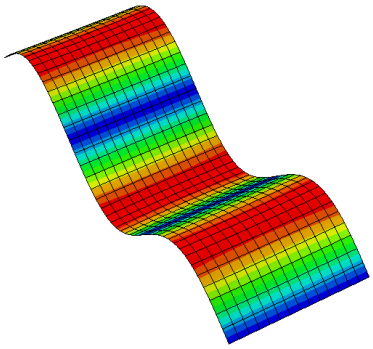

(e) Mode(3,1): 75.94 Hz.

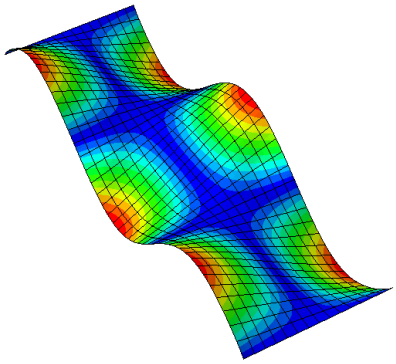

(f) Mode(3,2): 87.53 Hz.

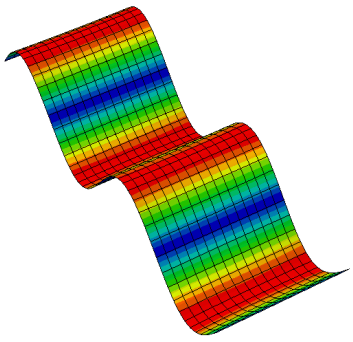

(g) Mode(4,1): 113.76 Hz.

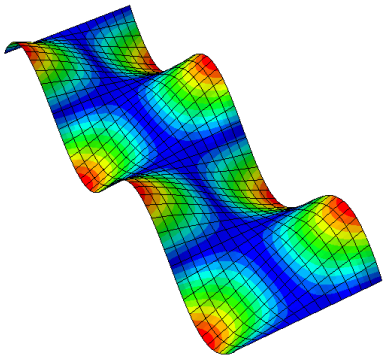

(h) Mode(4,2): 124.60 Hz.

Figure 6.3: The first eight eigenmodes of the Composite 2D model.

6.4 Differences in dynamic properties

The summary of the first eight eigenmodes is given in Table 6.4. In order to study and compare the eigenfrequencies between different models, we use the normalised relative frequency difference (NRFD) used according to Eq. 4.7.1. All models exhibit the same eigenmodes within the analysed frequency range, and all modes appear in the same order. The eigenfrequencies are lower for the High-fidelity model compared to the two alternative models, this becomes evident in Table 6.4.

It is clearly shown in Figure 6.4 that the largest error between the High-fidelity model and the alternative models exists for modes above one half sine wave in the y-direction. The bending motion of these modes are more complex as the bending acts about the two axes, resulting in larger discrepancies between the eigenfrequencies than for the simpler modes with bending in only one direction. When comparing modes with one half sine waves in the y-direction, the NRFD is comparatively small and seems to neither be increasing nor decreasing.

Table 6.4: Summary of the first eight eigenfrequencies of the three models arranged according to eigenmodes.

Mode	(1,1)	(1,2)	(2,1)	(2,2)	(3,1)	(3,2)	(4,1)	(4,2)
High-fidelity 3D model	11.47	19.62	39.60	48.24	74.81	82.81	112.21	119.67
Layered 3D model	11.53	22.45	39.93	52.21	75.62	87.33	113.65	124.70
Composite 2D model	11.57	22.43	40.12	52.33	75.94	87.53	113.76	124.60

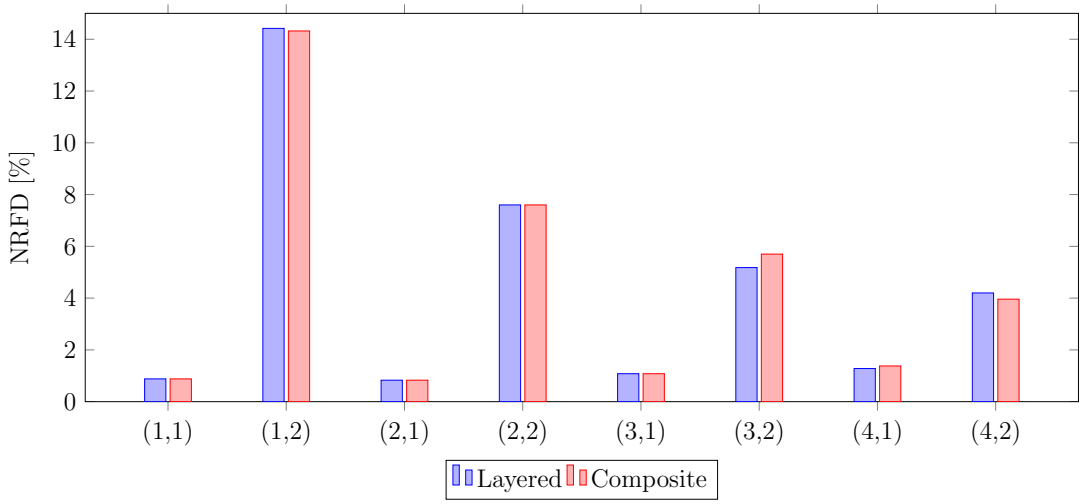

Figure 6.4: The NRFD between an alternative model and the High-fidelity 3D model, comparing the first eight eigenmodes, according to Eq. 4.7.1.

Table 6.5: Summary of the NRFD displayed in Figure 6.4

Mode	(1,1)	(1,2)	(2,1)	(2,2)	(3,1)	(3,2)	(4,1)	(4,2)
NRFD Layered 3D model [%]	0.88	14.42	0.83	7.60	1.08	5.18	1.28	4.20
NRFD Composite 2D model [%]	0.88	14.32	0.83	7.60	1.08	5.70	1.38	3.96

7 Effects on dynamic response

The dynamic response chapter is concerned with the dynamic response for the three models when subject to surface loads. Each model will be subject to two different load scenarios illustrated in Figures 7.1 and 7.3 respectively, where the dynamic response of each model is determined through a steady state analysis using Rayleigh and modal damping over a frequency range of 1–120 Hz, using 0.5 Hz increments. The steady state dynamic analysis provides the steady state response of the system subject to harmonic excitation at a given frequency. For each load position the velocity in two points will be evaluated. To discern the ability of the Layered and Composite models to replicate the dynamic behaviour of the High–fidelity model, the mobility in each measure point is compared. By evaluating the transfer and point mobility, the comparison aims to find any difference in vibration propagation throughout the structure depending on modelling approach. When evaluating the transfer mobility, the comparison is concerned with the complex velocity in the z–direction. Evaluation of a measure point coinciding with a load point is known as point mobility. The real part of the of the point mobility, when evaluating vibration velocity, is directly proportional to the amount of energy entering the evaluated structure [14]. This chapter is divided into different sections where:

Section 7.1: Addresses the damping used for the steady-state analyses.
Section 7.2: Considers a direct-solution steady-state analysis with Rayleigh damping.
Section 7.3: Considers a mode-based steady-state analysis using both Rayleigh and direct damping.
Section 7.4: Summarises the results from the steady-state analyses.

7.1 Damping

For the analyses two approaches to account for the damping have been considered, Rayleigh damping and direct modal damping, both being classical forms of damping. The damping parameters are selected from measured data of a scale-sized experimental structure representing a part of a two storey building. The model was analysed for frequencies up to 100 Hz, acquiring the damping parameters in Table 7.1.

Table 7.1: The damping parameters from the experimental structure in [8].

a_0	3.06
a_1	$3.22{\cdot}10^{-5}$
ζ	1.1 %

7.2 Direct solution - Effects on mobilities

The direct-solution steady state calculates the response of a system directly in terms of each individual degree of freedom, without reducing the system. This results in a computationally cumbersome yet accurate analysis. In this section only Rayleigh damping is considered.

7.2.1 Load position 1

The first load scenario evaluates a concentrated load placed in the centre of the CLT panel acting in the z–direction. The load position and measure points in relation to the CLT panel are illustrated in Figure 7.1. For each measure point separated from the load position the complex velocity is calculated and plotted, comparing the transfer mobility for the different models. Since load position one and measure point one are situated in the same node, the point mobility in measure point one will be evaluated in terms of the real part of the response, see Figure 7.2.

From the results in Figure 7.2, load position one excites eigenmode (1,1) and (3,1) according to the frequencies from Table 6.4. All models for load position one exhibit the same modal response with smaller velocity differences. In terms of both the transfer and point mobility, the maximum velocity difference is smaller for the Layered model than the Composite model when comparing it to the High-fidelity model.

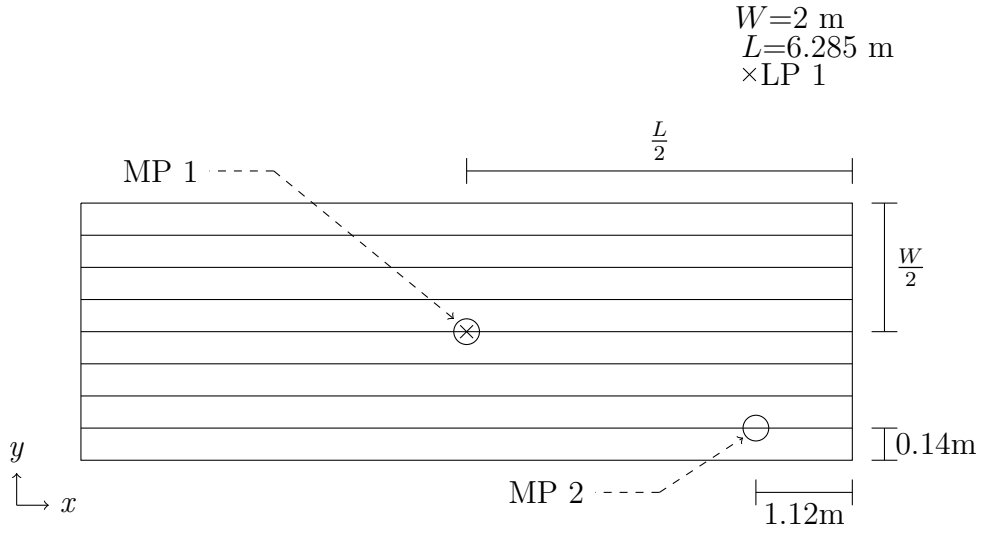

Figure 7.1: An illustration of the first load position, LP 1, and the position of the two measure points, MP 1 and MP 2, on the CLT panels surface.

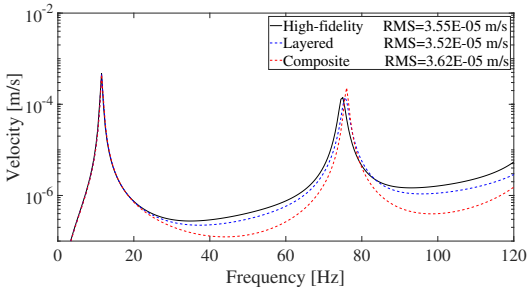

(a) The point mobility in MP 1, plotting the real part of the velocity in the z–direction.

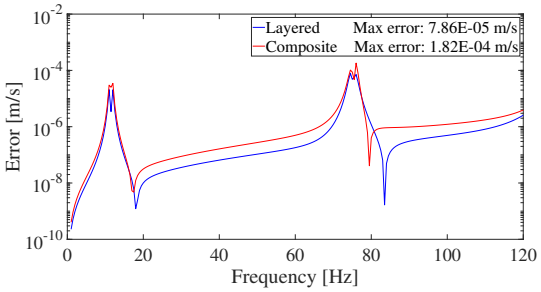

(b) The error in velocity comparing the alternative models with the High-fidelity model in (a).

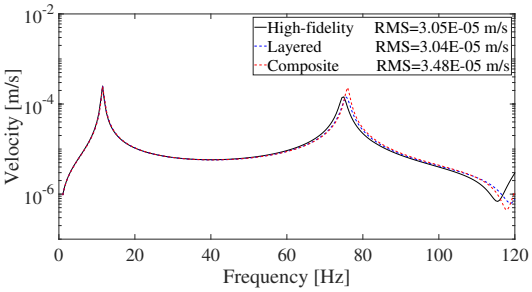

(c) The transfer mobility in MP 2, plotting the complex velocity response in the z–direction.

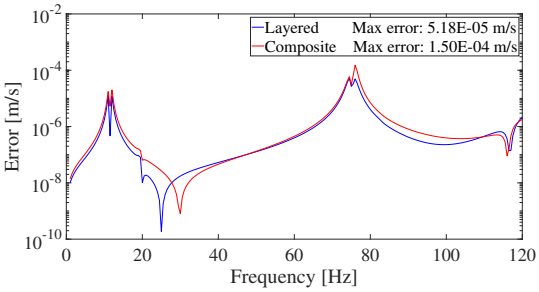

(d) The error in velocity comparing the alternative models with the High-fidelity model in (c).

Figure 7.2: Velocity response in MP 1 and MP 2, using direct-solution steady-state and LP 1.

7.2.2 Load position 2

The second load scenario evaluates the steady state response for a concentrated load placed on the surface of the CLT panel, see Figure 7.3. For load position two the load point does not coincide with a measure point, therefore only the transfer mobility will be evaluated in terms of the complex velocity in the z-direction. For each measure point and each model the direct steady state response will be calculated using Rayleigh damping according to the parameters in Section 7.1.

Measure point one excites eigenmode (1,1) and (3,1), the same as those in Figure 7.2, showing relatively small differences in velocity between models. The second measure point excites all eight modes below 120 Hz for the High-fidelity model. For modes below two sine waves in the y–direction all models closely replicate the same velocity response for a given frequency. While modes above one sine wave in the y–direction are exited at lower frequencies for the High-fidelity model than the alternative models. This is to be expected considering the error between eigenfrequencies for the three models in Figure 6.4.

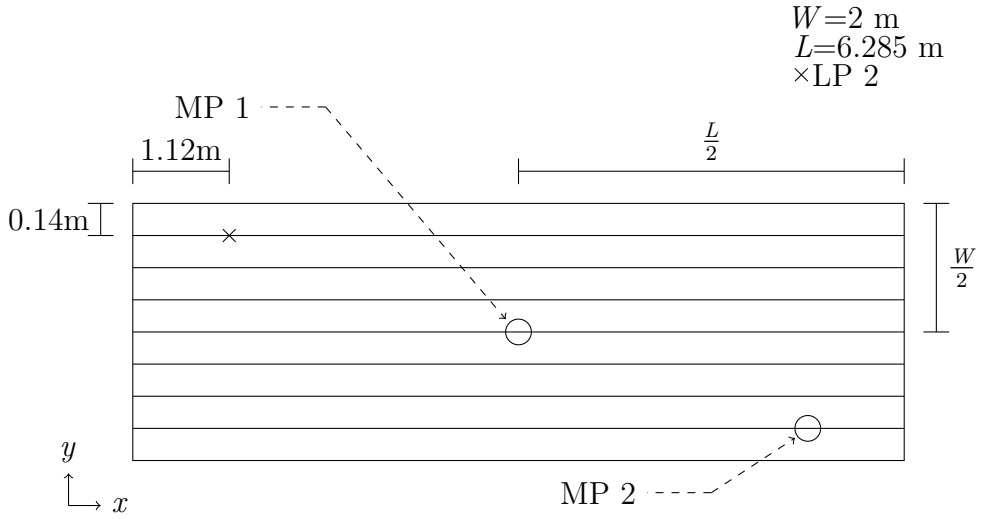

Figure 7.3: An illustration of the second load position, LP 2, and the position of the two measure points, MP 1 and MP 2, on the CLT panels surface.

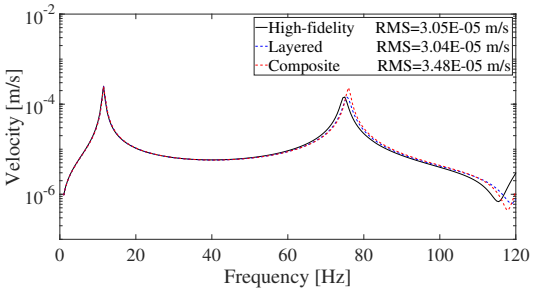

(a) The transfer mobility in MP 1, plotting the complex velocity response in the z–direction.

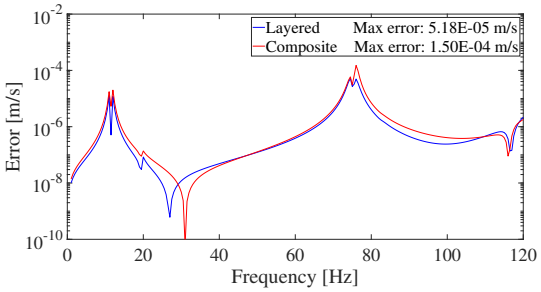

(b) The error in velocity comparing the alternative models with the High-fidelity model in (a).

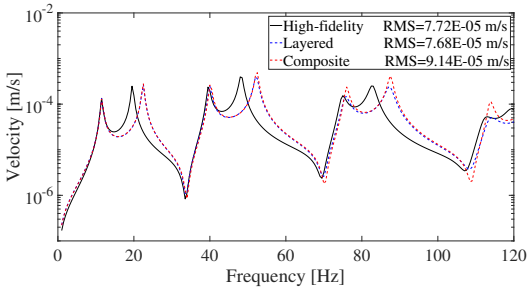

(c) The transfer mobility in MP 2, plotting the complex velocity response in the z–direction.

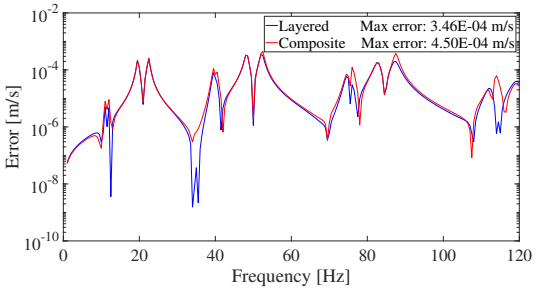

(d) The error in velocity comparing the alternative models with the High-fidelity model in (c).

Figure 7.4: Velocity response in MP 1 and MP 2, using direct-solution steady-state and LP 2.

7.3 Alternative analysis

For a mode-based steady state analysis, a sufficient amount of eigenmodes need to be extracted from an eigenvalue analysis to adequately describe the dynamic behaviour of the system. The use of modal superposition allows the deformation of the model to be explained in terms of individual modal contributions within a specified frequency range. The mode-based approach is less accurate than the direct-solution steady state, but is far less computationally cumbersome. For this section, the result of a mode-based steady state analysis for the alternative models are compared to the response of the direct-solution steady state response of the High-fidelity model.

7.3.1 Rayleigh damping

In Figure 7.5, mode-based steady state analyses with Rayleigh damping have been performed using four different frequency ranges for the High-fidelity model. The percentage error, described in Eq. 4.7.2, between the RMS value for the direct-solution and mode-based steady state analysis is plotted on the y–axis. Since an increase in number of eigenmodes used for the analysis results in an large set of equations to be computed, a smaller frequency range is preferred. From the error presented in Table 7.2, using a frequency range of 240 Hz (23 modes) results in a sufficiently accurate result. The results for the mode-based steady state analyses using Rayleigh damping and a frequency interval of 240 Hz are given in Figures 7.6–7.7.

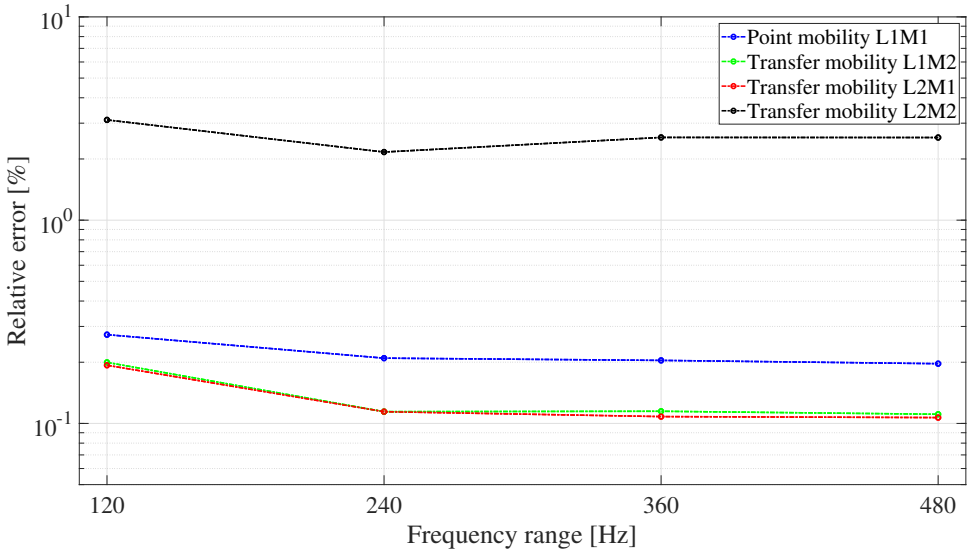

Figure 7.5: Plotting the relative error for the High-fidelity 3D model when comparing a direct-solution and mode-based steady state analysis using Rayleigh damping with four different frequency ranges. In the graph, L denotes the load position and M the measure point. The relative error is calculated according to Eq. 4.7.2.

Table 7.2: Summary of the errors in Figure 7.5, arranged according to the LP, MP and frequency range.

Scenario		**Relative error** [%]			
LP	MP	120 Hz	240 Hz	360 Hz	480 Hz
1	1	0.27	0.21	0.20	0.20
	2	0.20	0.11	0.11	0.11
2	1	0.19	0.11	0.11	0.11
	2	3.11	2.16	2.55	2.55

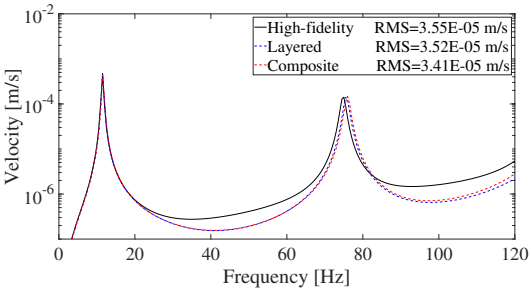

(a) The point mobility in MP 1, plotting the real part of the velocity response in the z–direction.

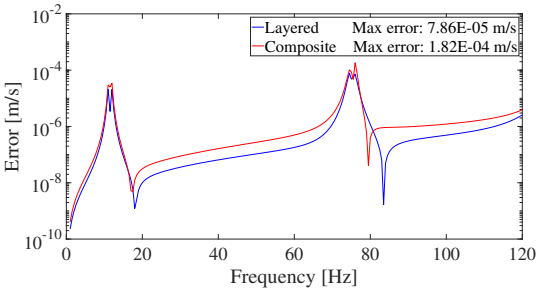

(b) The error in velocity comparing the alternative models with the High-fidelity model in (a).

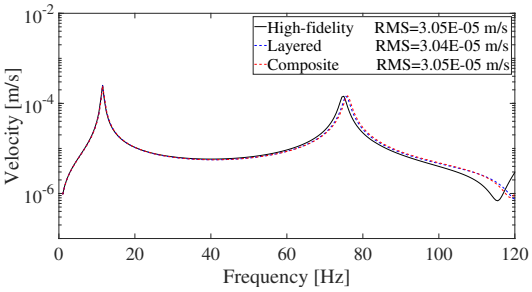

(c) The transfer mobility in MP 2, plotting the complex velocity response in the z–direction.

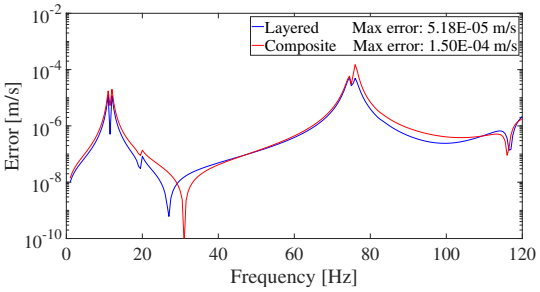

(d) The error in velocity comparing the alternative models with the High-fidelity model in (c).

Figure 7.6: Comparing the response of the High-fidelity model in LP 1, using a direct-solution steady state with Rayleigh damping, with a mode-based steady state for the alternative models using a 240 Hz frequency range and Rayleigh damping. The error calculated according to Eq. 4.7.3.

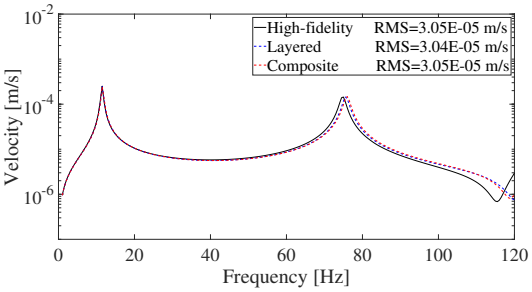

(a) The transfer mobility in MP 1, plotting the complex velocity response in the z–direction.

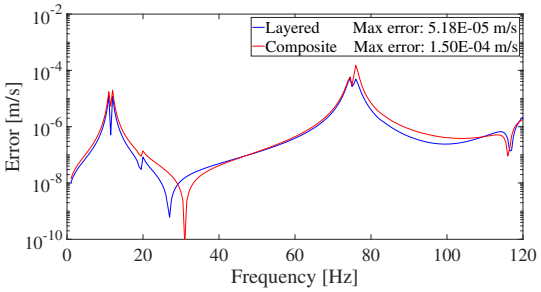

(b) The error in velocity comparing the alternative models with the High-fidelity model in (a).

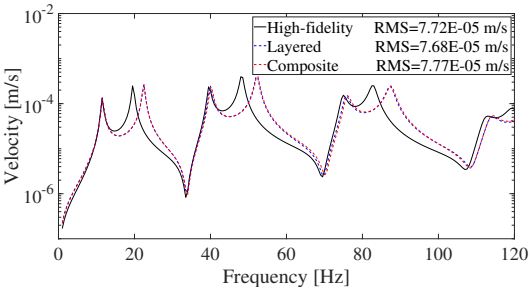

(c) The transfer mobility in MP 2, plotting the complex velocity response in the z–direction.

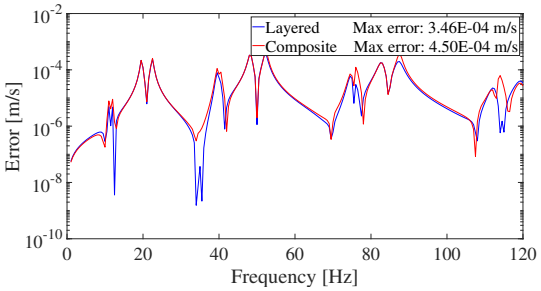

(d) The error in velocity comparing the alternative models with the High-fidelity model in (c).

Figure 7.7: Comparing the response of the High-fidelity model in LP 2, using a direct-solution steady state with Rayleigh damping, with a mode-based steady state for the alternative models using a 240 Hz frequency range and Rayleigh damping. The error calculated according to Eq. 4.7.3.

7.3.2 Direct modal damping

With the use of modal superpositioning, the damping ratio may be applied to each individual mode in a classical damping matrix. An ideal approach when dealing with systems with similar damping mechanisms distributed through the system. In Figures 7.8–7.9, a mode–based steady state analysis with the same damping ratio as the experiment in Section 7.1 is performed.

Although the results from the mode-based steady state analysis with modal damping clearly replicates the dynamic behaviour of the High-fidelity model for all measure points, the amplitude of the velocity response is far larger when using modal damping for the alternative models. This becomes evident when comparing the maximum velocity difference with the previous results. This difference in maximum velocity also translates into large differences in RMS values between different models. The frequency discrepancy between the High-fidelity model and the alternative model for modes above on half sine wave in the y-direction also exists when using modal damping, see Figure 7.9.

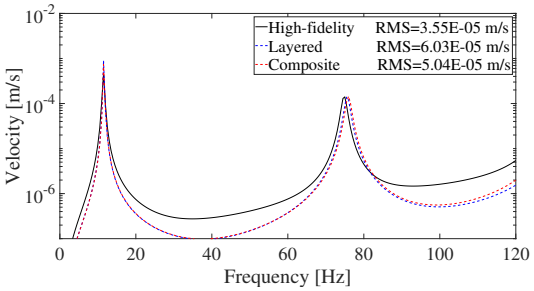

(a) The point mobility in MP 1, plotting the real part of the velocity response in the z–direction.

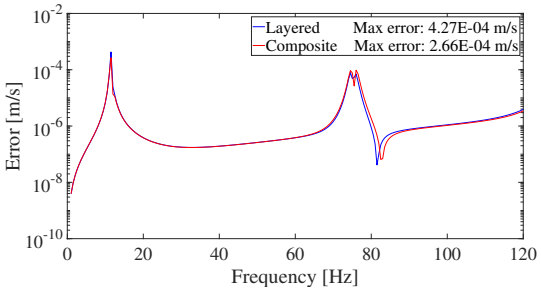

(b) The error in velocity comparing the alternative models with the High-fidelity model in (a).

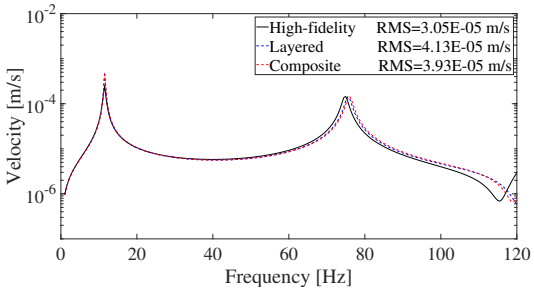

(c) The transfer mobility in MP 2, plotting the complex velocity response in the z–direction.

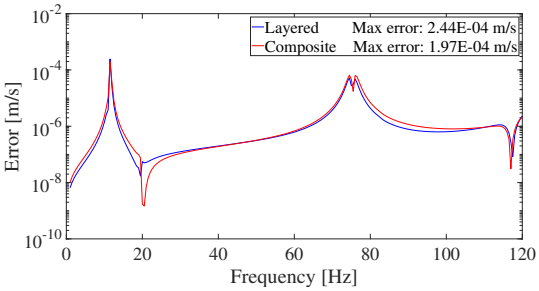

(d) The error in velocity comparing the alternative models with the High-fidelity model in (c).

Figure 7.8: Comparing the response of the High-fidelity model in LP 1, using a direct-solution steady state with Rayleigh damping, with a mode-based steady state for the alternative models using a 240 Hz frequency range and modal damping. The error calculated according to Eq. 4.7.3.

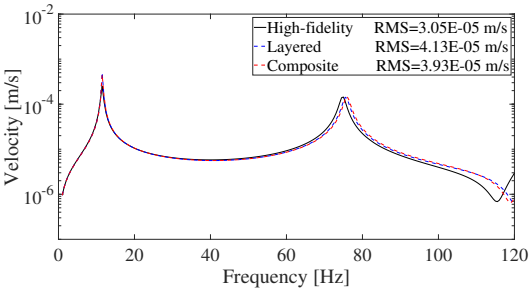

(a) The transfer mobility in MP1, plotting the complex velocity response in the z–direction.

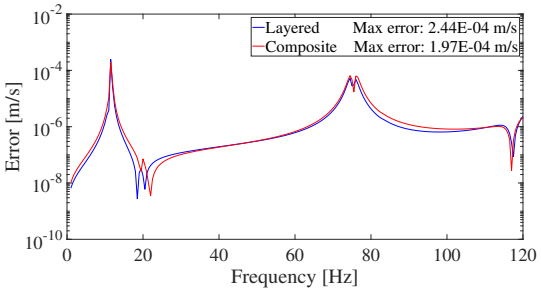

(b) The error in velocity comparing the alternative models with the High-fidelity model in (a).

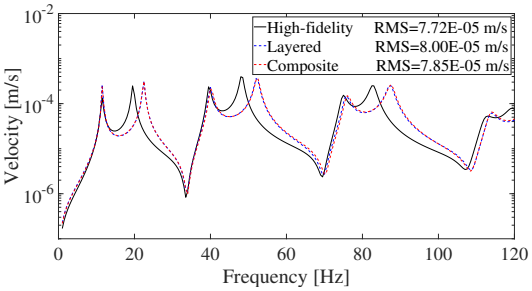

(c) The transfer mobility in MP2, plotting the complex velocity response in the z–direction.

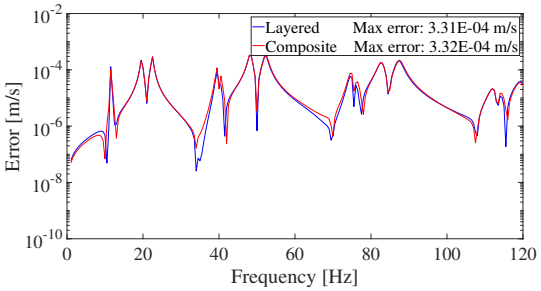

(d) The error in velocity comparing the alternative models with the High-fidelity model in (c).

Figure 7.9: Comparing the response of the High-fidelity model in LP 2, using a direct-solution steady state with Rayleigh damping, with a mode-based steady state for the alternative models using a 240 Hz frequency range and modal damping. The error calculated according to Eq. 4.7.3.

7.4 Response differences

In Table 7.3 the velocity RMS values for the three models are given ordered according to load position and measure point for a direct-solution steady state with Rayleigh damping. The error is described by comparing the RMS value for the alternative model with that of the High-fidelity model using Eq. 4.7.2. From the results in Table 7.3, the Layered model exhibits far smaller errors than the Composite model, the errors being below one percent for all measure points. The smallest error for the Composite model was achieved when evaluating the point mobility in measure point one during load position one. Incidentally, this was the measure point with largest error for the Layered model.

The RMS values from the two mode-based steady state analyses with Rayleigh and modal damping for the alternative models are given in Tables 7.4 and 7.5 respectively. The RMS value for the High-fidelity model using a direct-solution steady state analysis is used as a comparison for the alternative models. The RMS values for the Layered model directly replicates those in Table 7.3 when using Rayleigh damping, resulting in the same errors. The analyses for the Composite model resulted in smaller errors when using a mode-based steady state with Rayleigh damping than a direct solution analysis.

The mode–based steady state analysis with modal damping gives by far the largest errors between the High–fidelity and alternative models, with only one measure point giving relatively small errors.

Table 7.3: Summary of the RMS value for a direct-solution steady state analysis using Rayleigh damping according to the values in Section 7.1. The error describes the relative error when comparing the High-fidelity and an alternative model.

Scenario		**Root Mean Square** [10^{-5} m/s]			**Error**[%]	
LP	MP	High-fidelity	Layered 3D	Composite 2D	Layered 3D	Composite 2D
1	1	3.55	3.52	3.62	0.85	1.97
	2	3.05	3.04	3.48	0.33	14.10
2	1	3.05	3.04	3.48	0.33	14.10
	2	7.72	7.68	9.14	0.52	18.39

Table 7.4: Summary of the RMS value for the alternative models using a mode-based steady state analysis with Rayleigh damping according to the values in Section 7.1. The analysis is performed with a frequency range of 240 Hz. The error describes the relative RMS error when compared with the value of a direct-solution steady state analysis for the High-fidelity model.

Scenario		**Root Mean Square** [10^{-5} m/s]		**Error**[%]	
LP	MP	Layered 3D	Composite 2D	Layered 3D	Composite 2D
1	1	3.52	3.41	0.85	3.94
	2	3.04	3.05	0.33	0.00
2	1	3.04	3.05	0.33	0.00
	2	7.68	7.77	0.52	0.65

Table 7.5: Summary of the RMS value for the alternative models using a mode-based steady state analysis with modal damping according to the values in Section 7.1. The analysis is performed with a frequency range of 240 Hz. The error describes in the same manner as in Table 7.4.

Scenario		**Root Mean Square** [10^{-5} m/s]		**Error**[%]	
LP	MP	Layered 3D	Composite 2D	Layered 3D	Composite 2D
1	1	6.03	5.04	69.86	41.97
	2	4.13	3.93	35.41	28.85
2	1	4.13	3.93	35.41	28.85
	2	8.00	7.85	3.63	1.68

8 Discussion

In the investigation the High-fidelity 3D model is assumed to be the most accurate model. This assumption is due to the fact that the High-fidelity model is concerned with modelling each individual board and the gaps separating them horizontally for all seven layers, thus most accurately replicating a CLT panel. Therefore the two alternative models, the composite 2D and Layered 3D model, were evaluated by their ability to replicate the dynamical behaviour of the High-fidelity model.

Given the size and complexity of the High-fidelity model, the partitioning and modelling of each gap is very time-consuming. In total 193, each 0.2 mm wide, gaps needed to be modelled on a large CLT panel by manually entering the dimensions and position of them. This results in increased possibility of human error impacting the result. However, more than one High-fidlity model have been created, both showing the same exact modal behaviour.

8.1 Dynamic properties

Comparing the eigenfrequencies for the three numerical models, summarised in Table 6.4, the frequencies for the High-fidelity model are lower for all studied modes (below 120 Hz). The discrepancy for eigenfrequencies above one half sine wave in the y-direction are noticeably larger then those with only one half sine wave, this is clearly shown in Figure 6.4. The error for these eigenfrequencies also becomes smaller when comparing higher frequencies. The eigenfrequencies for both the Layered 3D and Composite 2D models seem to correspond quiet well with one another. But, it seems like the design simplification of omitting to model the gap between individual boards, regarding layers to act as solid layers, results in matching modal behaviour but higher eigenfrequencies. This increase in eigenfrequencies is assumed to be due to the higher stiffness of the alternative models, as the modelling of the gap directly decreases the stiffness of the High-fidelity model. If the eigenfrequencies for the alternative models are to correspond more accurately with the High-fidelity model, the material parameters for each solid layer may have to be altered to account for the gap.

8.2 Dynamic response

Considering the direct steady-state using Rayleigh damping, the Layered 3D model gave more accurate results than the Composite model, showing RMS errors below one percent for all measure points. This also indicates that using a Composite 2D model may be deemed a less accurate approach given the RMS errors shown in Table 7.3 when using a direct-solution steady-state analysis. This could be expected given the velocity error being larger for the Composite model than the Layered 3D model for all measure points, see Figures 7.2 and 7.4. As the Layered and the High-fidelity model are both 3D models, and the load for the Composite 2D model is projected on the plane located in the middle of the cross-section, it is expected that the former models

would more accurately replicate each other's dynamic response.

The use of a mode-based steady-state using Rayleigh damping results in smaller errors between the three models. Considering that all models exhibit the same mode sequence and mode shapes, a mode-based approach should result in small differences between the responses of the alternative models. This is due to the dynamic response being calculated in terms of modal contribution, see Section 4.5. From the results shown in Table 7.4, the error for both models can be considered quite small. Yet, once again, the Layered 3D model is more consistent with the results of the High-fidelity model. The small errors in shown in Table 7.4 indicates that the use of a mode-based steady-state with Rayleigh damping yields the smallest errors for the alternative models. This is a desired result as the mode-based steady-state requires less computational resources thanks to the approach of modal super-positioning and orthogonality of natural modes.

The mode based analysis with direct modal damping yielded the largest errors for the alternative models when compared to the direct-solution steady-state of the High-fidelity model, the results shown in Table 7.5. This is probably due to direct modal damping applying a constant viscous damping factor for all modes, while Rayleigh damping varies over different modes. When comparing the velocity errors shown in Figures 7.6 and 7.8, the error for mode (3,1) is about the same, while the error for mode (1,1) is considerably larger when using direct modal damping. This could be due to the difference in damping being larger for mode (1,1) than mode (3,1), as damping is the only difference between the two analyses.

8.3 General discussion

To model the adhesive as 0.2 mm thick void, in comparison to model the adhesive as a material with certain properties, will undoubtedly have some effect on the results, as this modelling approach results in the gaps contributing nothing to the stiffness or the mass matrices. At the same time there can be no form of wave propagation horizontally between each individual board. A possible problem derived from the decision of modelling the gaps in this way is the existence of elements with a high aspect ratio. The aspect ratio is the proportion between the longest and shortest edge of an element. To acquire reliable results the face of element should take a rectangular geometric form, and the aspect ratio should be as close to unity as possible, far too large aspect ratios may reduce the accuracy of the analysis [12]. Currently the maximum element face aspect ratio is 175.

9 Conclusion

9.1 Summary of results

The aim of this Master's dissertation is to evaluate the possibility of using less detailed alternative models and/or using computationally less cumbersome analyses when evaluating the dynamic response of CLT panels subject to internal loads. The results clearly indicate the possibility of using less detailed models when determining the dynamic response of CLT panels. The results in this dissertation concludes that:

- For eigenfrequencies up to 120 Hz, omitting to model the gaps results in a maximum NRFD of 14.4 % for modes above one half sine wave in the y-direction, while the maximum NRFD for all other modes does not exceed 1.4 %.
- The Layered 3D model with quadratic elements most accurately replicated the dynamic response of the High-fidelity 3D model when using a direct-solution steady state analysis with Rayleigh damping.
- The results from the mode-based analysis with Rayleigh damping indicate that both the Layered 3D and Composite 2D models are suitable alternatives for determining the dynamic response of a CLT panel when using modal analysis.
- The lower RMS velocity value for the Layered 3D model, when compared to the High-fidelity 3D model, indicates the importance of good adhesion between boards to reduce the dynamic response of a CLT panel.

9.2 Future work

From the work performed in this dissertation, suggestions for future research include:

- Evaluate different methods of modelling the adhesive, preferably using a experimental CLT panel as a reference. In this dissertation the adhesive is modelled as a 0.2 mm void, which may not accurately represent reality.
- This dissertation is concerned with only internal loads. Evaluating the possibility of using alternative less-detailed models and/or modal analysis to evaluate the dynamic response of a CLT panel subject to external loads, such as traffic loads.
- In this dissertation a numerical model is used as a reference model, assuming it replicates the behaviour of a CLT panel. Using an experimental model as a reference model would result in a more reliable result, and the exact Rayleigh damping parameters for the CLT panel could be assessed.

Bibliography

[1] Cecilia Avila et al. "Structural performance of finger-jointed black spruce lumber with different joint configurations". In: *Forest Products Journal* 53 (Sept. 2003).

[2] Eric Borgström and Johan Fröbel. *KL-trähandbok*. Stockholm: Swedish Wood, May 2017.

[3] Reinhard Brandner et al. *Cross laminated timber (CLT): overview and development*. Vol. 74. Jan. 2015. DOI: 10.1007/s00107-015-0999-5.

[4] Per Gunnar Burström. *Byggnadsmaterial*. Swedish. 2nd ed. Lund: Studentlitteratur AB, 2014.

[5] Prof. Dr. Sherwin Carlquist. *Comparative Wood Anatomy: Systematic, Ecological, and Evolutionary Aspects of Dicotyledon Wood*. 2nd ed. Springer Series in Wood Science. Springer-Verlag Berlin Heidelberg, 2001.

[6] I.P. Christovasilis et al. "Evaluation of the Mechanical Properties of Cross Laminated Timber with Elementary Beam Theories". In: *Construction and Building Materials* 122 (Sept. 2016), pp. 202–213.

[7] Henrik Danielsson. "Perpendicular to grain fracture analysis of wooden structural elements - Models and applications". PhD thesis. Lund University, 2013. URL: https://lup.lub.lu.se/search/ws/files/6343445/3633875.pdf.

[8] Ola Flodén, Kent Persson and Göran Sandberg. "A multi-level model correlation approach for low-frequency vibration transmission in wood structures". In: *Engineering Structures* 157 (Feb. 2018), pp. 27–41. DOI: 10.1016/j.engstruct.2017.11.062.

[9] Irene Gu, Henrik Andersson and Raúl Vicen. "Wood defect classification based on image analysis and support vector machines". In: *Wood Science and Technology* 44 (Nov. 2009), pp. 693–704. DOI: 10.1007/s00226-009-0287-9.

[10] John Nairn. "A numerical study of the transverse modulus of wood as a function of grain orientation and properties". In: *Holzforschung* 61 (June 2007), pp. 406–413. DOI: 10.1515/HF.2007.079.

[11] Juan Negreira. "Vibroacoustic performance of wooden buildings: Prediction and Perception". PhD thesis. Engineering Acoustics, Apr. 2016. ISBN: 978-91-7623-642-0.

[12] Niels Ottosen and Hans Petersson. *Introduction to the finite element method*. Great Britain: Practice Hall, 1992.

[13] Kent Persson. "Micromechanical Modelling of Wood and Fibre Properties". PhD thesis. Dec. 2000. DOI: 10.13140/RG.2.1.1389.7685.

[14] Peter Persson, Ola Flodén and Björn Pedersen. "Predicting vibroacoustic performance of thin-walled lightweight structures during conceptual design". In: *Finite Elements in Analysis and Design* 169 (Feb. 2020). DOI: 10.1016/j.finel.2019.103342.

[15] Matti Ristinmaa and Niels Ottosen. *The Mechanics of Constitutive Modeling*. 1st ed. Elsevier Science, Sept. 2005.

[16] Erik. Serrano. "Adhesive Joints in Timber Engineering. Modelling and Testing of Fracture Properties". In: Report TVSM (2000).

[17] Michael Smith. *ABAQUS/Standard User's Manual, Version 6.9*. English. United States: Dassault Systémes Simulia Corp, 2009.

[18] Swedish Ministry of Enterprise, Energy and Communications. "Mer trä i byggandet - Underlag för en nationell strategi att främja användning av trä i byggande". Swedish. In: (2004). DOI: Ds2004:1.

[19] Swedish Wood. *Design of timber structures : Structural aspects of timber construction*. 2nd ed. Stockholm: Swedish Wood, Oct. 2016.

[20] Swedish wood. *Återvinning av träprodukter*. Swedish. URL: https://www.traguiden.se/om-tra/miljo/miljoeffekter/miljoeffekter/atervinning-av-traprodukter/?previousState=1f. accessed: 19.03.2020.

[21] Swedish wood. *The forest and sustainable forestry*. Swedish. URL: https://www.swedishwood.com/wood-facts/about-wood/wood-and-the-environment/the-forest-and-sustainable-forestry/. accessed: 30.03.2020.

[22] University of Kentucky College of Agriculture. *An introduction to wood anatomy characteristics common to softwoods & hardwoods*. 1997. URL: http://www2.ca.uky.edu/agcomm/pubs/for/for59/for59.pdf. accessed: 19.03.2020.

[23] E. Ussher et al. "Predicting effects of design variables on modal response of CLT floors". In: *Structures* 11 (Aug. 2017), pp. 40–48.